

1 **Precipitation of Relativistic Electrons Under Resonant**  
2 **Interaction with Electromagnetic Ion-Cyclotron Wave**  
3 **Packets**

4 **V. S. Grach<sup>1</sup> and A. G. Demekhov<sup>2,1</sup>**

5 <sup>1</sup>Institute of Applied Physics, Russian Academy of Sciences

6 <sup>2</sup>Polar Geophysical Institute

7 <sup>1</sup>46, Ul'yanov st., 603950, Nizhny Novgorod, Russia

8 <sup>2</sup>26a, Academgorodok st., 184209, Apatity, Russia

9 **Key Points:**

- 10 • Nonlinear resonant interaction with EMIC waves can either increase or decrease  
11 electron pitch angle  
12 • For some energies pitch angle distribution stays isotropic, precipitating fluxes at  
13 strong diffusion limit  
14 • For higher energies precipitating fluxes correspond to weak diffusion and agree with  
15 quasi-linear theory

---

Corresponding author: V.S. Grach, vsgrach@ipfran.ru

**Abstract**

We use numerical simulations to study the resonant interaction of relativistic electrons with rising-frequency EMIC wave packets in the  $H^+$  band. We find that precipitating fluxes are formed by quasi-linear interaction and several nonlinear interaction regimes having opposite effects. In particular, the direct influence of Lorentz force on the particle phase (force bunching) decreases precipitation for particles with low equatorial pitch angles (up to  $15\text{--}25^\circ$ ), and can even block it completely. Four other nonlinear regimes are possible: nonlinear shift of the resonance point which can cause pitch angle drift in both directions; phase bunching that slightly increases pitch angle for untrapped particles; directed scattering that strongly decreases pitch angle for untrapped particles, and particle trapping by the wave field that decreases pitch angle. The evolution of the equatorial pitch-angle distribution during several passes of particles through the wave packet is studied. The precipitating fluxes are evaluated and compared with theoretical estimates. We show that strong diffusion limit is maintained for a certain range of energies by a wave packet with realistic amplitude and frequency drift. In this case, the quasi-linear theory strongly underestimates the precipitating flux. With increasing energy, the precipitating fluxes decrease and become close to the quasi-linear estimates.

**1 Introduction**

The loss of relativistic radiation belt electrons has been observed and studied theoretically for a number of years (Thorne & Kennel, 1971; Millan & Thorne, 2007; Morley et al., 2010; Engebretson et al., 2015). The resonant interaction of relativistic electrons with electromagnetic ion-cyclotron (EMIC) waves is believed to be one of the main causes of this precipitation.

Initially, resonant interaction of relativistic electrons with EMIC waves has been analyzed within the framework of the quasi-linear theory (Summers & Thorne, 2003; Jordanova et al., 2008; Shprits et al., 2009). However, along with the noise bursts of EMIC waves, quasi-monochromatic wave packets (pearls or hydromagnetic chorus emissions) with frequencies of several Hz are often observed and their amplitudes, even moderate ones, can be high enough to ensure strongly nonlinear interaction (Kangas et al., 1998; Demekhov, 2007; Engebretson et al., 2007; Engebretson et al., 2008; Pickett et al., 2010). Pearl emissions (periodic sequences of quasi-monochromatic wave packets with periods about 100 s and increasing frequency inside each packet) are explained by a passive mode locking regime of the ion cyclotron instability (Belyayev et al., 1984; Belyaev et al., 1987; Demekhov, 2007; Trakhtengerts & Rycroft, 2008). Hydromagnetic chorus emissions or EMIC triggered emissions (Pickett et al., 2010) are similar in structure to whistler mode (ELF/VLF) chorus emissions (e.g. (Santolik et al., 2003)), and they are probably generated by a similar mechanism (Trakhtengerts, 1995). Nonlinear models of hydromagnetic chorus emissions were developed by Trakhtengerts and Demekhov (2007); Omura et al. (2010); Shoji et al. (2011). It is also worth noting that the observed loss of the outer radiation belt (Morley et al., 2010) can be too fast to be explained by quasi-linear diffusion rates.

Albert and Bortnik (2009) analyzed nonlinear interaction of relativistic electrons with an EMIC wave with a constant frequency. They showed the possible role of two nonlinear regimes: phase bunching without trapping, which leads to rapid pitch angle increase and thus can decrease the precipitating flux, and particles trapping by the wave field, which results in decreasing pitch angle. Artemyev et al. (2015) showed that trapping by the EMIC wave is stable with respect to non-resonant magnetic field fluctuations.

Nonlinear interaction of relativistic electrons with a model EMIC wave packet, corresponding to the emission with rising frequency, has been studied through theoretical analysis and test particle simulations in (Omura & Zhao, 2012, 2013; Kubota & Omura,

2017; Grach & Demekhov, 2018a, 2018b). Kubota and Omura (2017) showed that combined scattering process of the nonlinear wave trapping and another nonlinear regime 'SLPA' (Scattering at Low Pitch Angle) can lead to the rapid loss of relativistic electrons. The authors explained 'SLPA'-regime by the Lorentz force term in the equation for the particle phase (hereafter termed force bunching).

Grach and Demekhov (2018a, 2018b) have shown that a strong non-diffusive decrease of the pitch angle of untrapped electrons can also occur for fairly high pitch angles. This effect, called directed scattering, is not related to the force bunching and occurs for a small group of particles that spend a long time near the separatrix on the phase plane far from the saddle point, i.e., in the region where the phase is opposite to the phase-bunched particles.

Long time evolution of particle distribution function as a result of nonlinear resonant interaction with a monochromatic wave (various modes) was studied by Artemyev et al. (2017, 2018). A generalized Fokker-Planck equation, allowing for nonlinear regimes, was obtained; its analytical solutions have been validated by results of test particle numerical simulations. Two nonlinear regimes were taken into account: phase bunching (nonlinear scattering) and wave trapping; those regimes cause particles fast transport in phase space in the opposite directions. As a result, the Gaussian-shaped particle distribution function was shown to reach almost isotropic stationary solution. Kubota and Omura (2017) analyzed long time evolution of particle distribution in equatorial pitch angles under the resonant interaction and found echoes of electron depletion by the localized EMIC wave packets with rising frequency. They excluded particles with initial equatorial pitch angles near the loss cone from the consideration to avoid quasi-linear effects.

In this paper, we study the evolution of pitch angle distribution function during several passes of particles through the EMIC wave packet with rising frequency. We take into account particles with low initial equatorial pitch angles (close to the loss cone) and show that such particles play an important and peculiar role in the formation of precipitated flux. We also calculate precipitated fluxes, and compare them with theoretical estimates obtained from quasi-linear equations, and analyze the roles of quasi-linear interaction and several nonlinear regimes in the flux formation.

We show that under sufficiently high but realistic wave amplitude and relatively low refractive index force bunching can be very significant for the particles close to the loss cone. For these particles, force bunching can increase pitch angles and even block the precipitation completely from a noticeable range of low pitch angles. We show that for the most part of the considered parameters the pitch angle distribution in the vicinity of the loss cone is close to isotropic. The precipitating fluxes are formed as a result of several interaction regimes with opposite effects. The simulated fluxes are close to quasi-linear theoretical estimates when these estimates are applicable, and may significantly exceed them in other cases.

Next we describe the simulation model. In section 3.1, we summarize known results about the possible interaction regimes for a single electron pass through the wave packet and apply them to the chosen parameters, and also consider some new aspects of the force bunching. In section 3.2, we discuss the role of various interaction regimes in forming the precipitating flux during multiple passes through the wave packet. In section 4, we discuss the evolution of the pitch-angle distribution, obtain precipitating fluxes and compare the results with theoretical estimates. Section 5 is devoted to discussion and conclusions.

## 2 Simulation Model

### 2.1 Theory

For parallel-propagating EMIC waves, the resonant interaction with electrons is possible only at the anomalous cyclotron resonance, and the resonance condition is written as follows:

$$\Delta = \omega - kv_{\parallel} + \Omega_c/\gamma = 0, \quad (1)$$

where  $\omega$  and  $k$  are wave frequency and number, respectively,  $v_{\parallel}$  is field-aligned velocity,  $\Omega_c = eB_0/mc$ ,  $B_0$  is geomagnetic field,  $e > 0$  is elementary charge,  $\gamma = \sqrt{1 + [p/(mc)]^2}$ ,  $m$  and  $p$  are the electron rest mass and momentum, respectively.

If the external field inhomogeneity is smooth, the wave magnetic field amplitude,  $\mathbf{B}_w$ , is small ( $B_w \ll B_0$ ) and wave characteristics vary slowly in time and space on the scales of  $2\pi/\Omega_c$  and  $2\pi/k$ , respectively, the resonant interaction of a test electron with EMIC wave can be described by the following equations:

$$\frac{dW}{dt} = -ev_{\perp}|E_w|\sin\Psi; \quad (2)$$

$$\frac{dI_{\perp}}{dt} = -\frac{2e}{mB_0}p_{\perp}(1 - n_{\parallel}\beta_{\parallel})|E_w|\sin\Psi; \quad (3)$$

$$\frac{d\Psi}{dt} = -\Delta - \frac{e}{p_{\perp}}(1 - n_{\parallel}\beta_{\parallel})|E_w|\cos\Psi; \quad (4)$$

$$\frac{dz}{dt} = \frac{p_{\parallel}}{m\gamma}. \quad (5)$$

Here the subscripts  $\perp$  and  $\parallel$  denote projections to the transverse and parallel directions with respect to  $\mathbf{B}_0$ , respectively,  $E_w$  is slowly changing wave electric field amplitude,  $n_{\parallel} = kc/\omega$ ,  $\Psi$  is the gyrophase defined as the angle between  $\mathbf{p}_{\perp}$  and  $-\mathbf{B}_w$ ,  $\beta_{\parallel} = v_{\parallel}/c$ ,  $W = (\gamma-1)mc^2$  and  $I_{\perp} = p_{\perp}^2/(mB_0)$  are the electron kinetic energy and the first adiabatic invariant respectively, and  $z$  is coordinate along the geomagnetic field with  $z = 0$  corresponding to the equator. In the right-hand side of equation (4) the first term represents inertial, or kinematic bunching, while the second one represents the direct influence of Lorentz force on the particle phase (force bunching).

The resonant interaction with EMIC waves,  $\omega \ll \Omega_c$ , is possible only for  $k_{\parallel}v_{\parallel} > 0$  and the change in electron energy  $W$  will be insignificant:  $\gamma \approx \text{const}$  (Bespalov & Trakhtengerts, 1986; Albert & Bortnik, 2009). The interaction result is described by the change in the adiabatic invariant  $I_{\perp}$  or equatorial pitch angle  $\Theta_L$ ,  $\mu = \sin^2\Theta_L = (p_{\perp}^2/p^2)(B_L/B_0)$ .

Particle behavior (interaction regime) is determined by the inhomogeneity parameter  $\mathcal{R} = \sigma_R R$  (Karpman et al., 1974; Albert, 1993, 2000; Albert & Bortnik, 2009; Kubota & Omura, 2017; Grach & Demekhov, 2018a), where  $\sigma_R = \pm 1$  determines the effective inhomogeneity sign, and

$$R = \frac{|d\Delta/dt|}{\Omega_{\text{tr}}^2}. \quad (6)$$

Here  $\Omega_{\text{tr}}^2$  is frequency of electron oscillations in the wave field near the effective potential minimum (Grach & Demekhov, 2018a; Demekhov et al., 2006). Under real conditions, the parameter  $R$  changes both in time and in space. These changes are associated both with medium inhomogeneity (including changes in the wave packet frequency and amplitude) and nonlinear changes in the particle parameters during the interaction. However, the main features of the particle motion can be categorized based on the  $R$  values calculated at the resonance point in the linear approximation. For  $R > 1$ , the trajectories of all particles on the phase plane are open (all particles are untrapped), and for  $R < 1$  there is a minimum of the wave effective potential, i.e. particle trapping by the

151 wave field is possible. The phase trajectories of the trapped particles are closed. For res-  
 152 onant interaction of electrons with EMIC wave packet, which is generated near the equa-  
 153 tor and propagates away from it, the effective inhomogeneity is negative. Hereafter, we  
 154 assume  $\sigma_R = -1$ .

155 The case of  $R \gg 1$  corresponds to the quasi-linear regime. In this case the change  
 156 in particle equatorial pitch angle (and energy) is determined by the resonance phase (Albert,  
 157 2000; Albert & Bortnik, 2009; Grach & Demekhov, 2018a):

$$\Delta\mu = K_\mu \sin(\Psi_{\text{res}} - \pi/4). \quad (7)$$

158 Here  $\mu = \sin^2 \Theta_L$ ,

$$K_\mu = \frac{2e}{mB_0} |p_\perp (1 - n_{||}\beta_{||}) E_w| \sqrt{\frac{2\pi}{d^2\Psi/dt^2}}. \quad (8)$$

159 All parameters of particles, plasma, and waves in (8) are calculated at the resonance point  
 160 on the unperturbed trajectory. In the quasi-linear regime, the resonance phase  $\Psi_{\text{res}}$  lin-  
 161 early depends on the initial phase  $\Psi_0$ , so for the particles with initial phases uniformly  
 162 distributed in  $[0, 2\pi]$ ,  $\Psi_{\text{res}}$  will also be uniformly distributed in  $[0, 2\pi]$ . For such ensem-  
 163 ble of particles equatorial pitch angle diffusion takes place:

$$\langle \Delta\mu \rangle^{\text{lin}} = 0; \quad (9)$$

164

$$\langle \Delta\mu \rangle_{\text{rms}}^{\text{lin}} = \sqrt{\langle (\Delta\mu^{\text{lin}} - \langle \Delta\mu \rangle^{\text{lin}})^2 \rangle} = K_\mu / \sqrt{2}. \quad (10)$$

165 Hereafter, angle brackets denote phase averaging.

166 For  $R \leq 1$ , the resonant interaction is nonlinear, which leads to drift in pitch an-  
 167 gles for both trapped and untrapped particles. The drift direction is determined by the  
 168 interaction regime and the sign of effective inhomogeneity.

169 Albert (1993, 2000) have shown analytically that when  $R \ll 1$  the resonance phase  
 170 for untrapped particles can take a limited range of values (for  $R \rightarrow 0$ ,  $\Psi_{\text{res}} \approx \pi$ ) and  
 171 the resulting change in particle parameters doesn't depend on the initial phase. For  $\sigma_R =$   
 172  $-1$ , this phase bunching without trapping leads to pitch angle increase (Albert & Bort-  
 173 nik, 2009; Grach & Demekhov, 2018a, 2018b). In some papers (Artemyev et al., 2017,  
 174 2018) this regime is called nonlinear scattering. Numerical simulations show (Kubota  
 175 & Omura, 2017; Grach & Demekhov, 2018a, 2018b) that for not too small  $R < 1$  there  
 176 can exist a small group of untrapped particles whose equatorial pitch angle decreases sig-  
 177 nificantly. This group of particles crosses the separatrix on the phase plane far from the  
 178 saddle point (near the reflection point), i.e., in the region where the phase is opposite  
 179 to the phase-bunched particles. The second order resonance condition is approximately  
 180 fulfilled for these particles ( $d^2\Psi/dt^2 \approx 0$ ), and they spend a long time in the separa-  
 181 trix region, which leads to noticeable pitch angle decrease (detailed analysis of the phase  
 182 plane can be found in (Grach & Demekhov, 2018a)). We term this regime directed scat-  
 183 tering to distinguish it from nonlinear scattering/phase bunching. The third regime is  
 184 the particle trapping by the wave field. In this case the equatorial pitch angle also sig-  
 185 nificantly decreases.

186 Nonlinear effects can also take place for  $R \geq 1$ . For low pitch angles and large  $K_\mu$   
 187 in the case of  $K_\mu > \mu$  quasi-linear estimate (7) is inapplicable (or is applicable only for  
 188 particles with certain initial phases). Force bunching (which is neglected in (7)) also be-  
 189 comes significant for low  $\Theta_L$  (small  $\mu$ , i.e., particles near the loss cone). If the wave am-  
 190 plitude is high enough, then the resonance point is shifted during the interaction. It leads  
 191 to particles with the same initial pitch angle but different initial phases having differ-  
 192 ent resonance points, and, consequently, different values of  $R$  and  $K_\mu$ . If the dependence  
 193  $K_\mu(\mu)$  is significant, that can cause drift in  $\mu$  ( $\langle \Delta\mu \rangle \neq 0$ ).

194

## 2.2 Wave packet model and plasma parameters

195

196

197

198

199

200

EMIC waves are observed in a wide range of geocentric distances  $L = 3\text{--}10$  and longitudes  $05\text{--}21$  MLT (Anderson & Hamilton, 1993; Fraser & Nguyen, 2001; Loto'aniu et al., 2005; Usanova et al., 2012; Keika et al., 2013). The frequencies of quasi-monochromatic wave packets (pearls or hydromagnetic chorus emissions) are in the range  $1\text{--}3$  Hz. Typical wave amplitudes are about  $1\text{--}2$  nT (Mursula, 2007; Engebretson et al., 2007; Engebretson et al., 2008), but values as large as  $11$  nT were observed (Engebretson et al., 2015).

201

202

203

In this paper, we consider the wave packets representing hydromagnetic chorus emissions with rising frequency, between the  $\text{He}^+$  and proton gyrofrequencies (i.e., in the  $\text{H}^+$  band).

204

205

206

The dipole model of geomagnetic field is used with McIlwain parameter  $L = 5.69$ . Cold plasma density at equator is  $N_e = 30 \text{ cm}^{-3}$ , proton density at equator is  $N_{\text{H}^+} = 0.95N_e$ , helium and oxygen densities at equator are  $N_{\text{He}^+} = N_{\text{O}^+} = 0.025N_e = 0.025N_e$ .

207

208

209

210

We consider a single wave packet with initial length along the geomagnetic field line  $L_{\text{pt}} \approx 4500$  km. The frequency grows linearly from  $f_{\text{fe}} = 1.025$  Hz ( $\approx 0.38f_H$ , where  $f_H$  is proton gyrofrequency) at the front edge to  $f_{\text{te}} = 2.3$  Hz ( $\approx 0.85f_H$ ) at the trailing edge  $z_{\text{te}} \approx -1$  km.

211

212

213

214

215

216

217

218

219

220

221

222

223

The result of the resonance interaction can significantly depend on the amplitude profile (Tao et al., 2012, 2013; Kubota & Omura, 2017; Grach & Demekhov, 2018a, 2018b). Tao et al. (2012, 2013) discussed the influence of the wave packet fine structure and the role of the subpackets. Here we follow (Grach & Demekhov, 2018a, 2018b), and consider an isolated wave packet with two initial profiles of the magnetic wave amplitude: constant  $B_w = B_w^{\text{max}} = \text{const}$  (flat packet) and Gaussian-shaped  $B_w = B_w^{\text{max}} \exp(-(z - z_{\text{mp}})^2 / \sigma_{\text{pt}}^2)$  (Gaussian packet). Here  $z_{\text{mp}}$  is the middle point of the packet, maximum initial amplitude is chosen as  $B_w^{\text{max}} = 3$  nT and  $\sigma_{\text{pt}} \approx L_{\text{pt}}/6$ . The Gaussian shape seems more realistic, but we consider both shapes in order to demonstrate the nonlinear effects more clearly and discuss the influence of amplitude profile. The chosen parameters are typical for EMIC events observed by Van Allen Probes in  $\text{H}^+$  band (e.g., (Engebretson et al., 2015)) and specifically represent the case observed during a SC event of 14 September 2017, which was discussed by Yahnin et al. (2019).

224

225

226

227

228

229

230

231

232

233

234

235

236

237

The packet propagates away from the equator ( $z$  is positive and increases). The evolution of the packet (in the cold plasma approximation) is taken into account in the simulation. The simulation time is limited to  $6.5$  s; at later times the dispersion distortion of the packet due to the presence of  $\text{He}^+$  ions becomes significant. This choice of simulation time also allows us to neglect the effect of magnetic drift on the electron distribution function in a given flux tube. Indeed, the typical transverse size of EMIC wave packets known from spaceborne and ground-based measurements is about  $2^\circ$ . For the chosen energy range  $W_0 = 1.4\text{--}3.0$  MeV, the drift time across the packet will be  $17\text{--}36$  s, which is more than two times longer than simulation time. The energy range is chosen based on  $R$  values for Gaussian packet (see below). The initial equatorial pitch angle range is  $\Theta_{L0} = 4\text{--}80^\circ$ . From below it is limited by the loss cone (for  $L = 5.69$ ,  $\Theta_{Lc} \approx 3.1^\circ$ ) and from above by the condition of the resonant interaction for particles within the specified energy range. For particles in the considered energy range, the simulation time corresponds to  $10\text{--}20$  bounce periods.

238

239

240

241

242

243

244

The system (2)–(5) was solved numerically by Bogacky-Shampine variant of the Runge-Kutta method. Calculations were done for 8 values of energy in the specified range ( $1.4; 1.6; 1.8; 2.0; 2.25; 2.5; 2.75$  and  $3.0$  MeV), 77 values of equatorial pitch angle (step of  $1$  degree) and 180 values of the initial phase (uniformly in  $[0, 2\pi]$ ). Thus, for every energy, the trajectories of 13860 particles were calculated. At the moment  $t = 0$  all particles are placed at the trailing edge of the packet with positive longitudinal velocities. As is shown below, this is insignificant for the results, since the particles are spread over

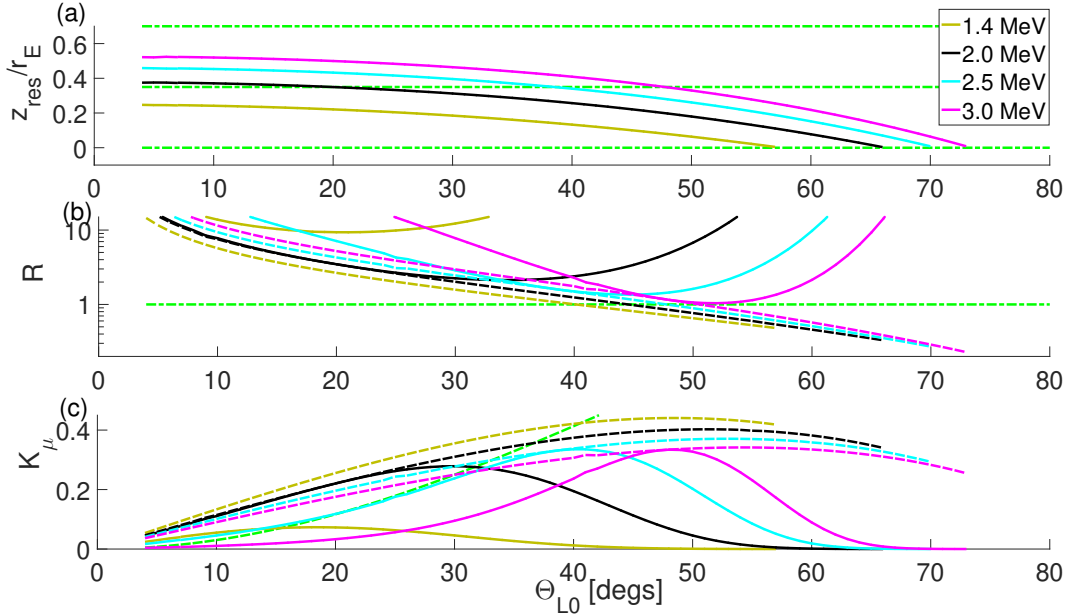


**Figure 1.** Resonance point location  $z_{\text{res}}$  normalized to the Earth radii  $r_E$  (a), unperturbed value of the inhomogeneity parameter  $R$  (b), and parameter  $K_\mu$  (c) for a flat packet (dashed lines) and a Gaussian packet (solid lines). Green dash-dotted lines show the edges and middle of the packet (a),  $R = 1$  (b) and the line  $K_\mu = \mu$  (c).

245 the field line in 3–4 bounces. If the particle is in the loss cone after leaving the packet  
 246 ( $\Theta_L < \Theta_{Lc}$ ), then the simulation for this particle is stopped.

### 247 3 Specific features of Interaction Regimes

#### 248 3.1 Single pass through the wave packet

249 In this section we will analyze the interaction regimes for a single electron pass through  
 250 the wave packet. The results of this analysis combined with knowledge of wave packet  
 251 evolution will allow us to qualitatively understand multi-pass results.

##### 252 3.1.1 Inhomogeneity parameter

253 The resonance point locations and the unperturbed values of parameters  $R$  and  $K_\mu$   
 254 for various initial equatorial pitch angles and the electron energies are shown in Figure 1  
 255 (for the initial packet location,  $t = 0$ ). The values of  $K_\mu$  are fairly large even for lin-  
 256 ear conditions ( $R > 1$ ), which results from relatively low plasma density. The latter de-  
 257 termines the EMIC wave refractive index entering formula (8).

258 The resonance point is shifted to the packet trailing edge with increasing  $\Theta_L$ . For  
 259 a flat wave packet, the inhomogeneity parameter  $R$  decreases with  $\Theta_L$  and increases with  
 260 energy  $W_0$ , while for a Gaussian wave packet  $R$  has a minimum in  $\Theta_L$  which location  
 261 depends on particle energy. Parameter  $K_\mu$  has a maximum in  $\Theta_L$ , but for a flat packet  
 262 the  $K_\mu$  decrease at high  $\Theta_L$  is insignificant.

263 Quantitatively, nonlinear regimes  $R \leq 1$  for a Gaussian packet can be observed  
 264 only for highest energies from the considered range and for a narrow pitch angle range  
 265 near  $50^\circ$ . For a flat packet,  $R \leq 1$  regimes can be observed for all energies, but for rel-

266 atively high pitch angles  $\Theta_L > 40^\circ$ . At the same time, as the dependence  $K_\mu(\Theta_L)$  shows,  
 267 various nonlinear effects are possible for  $R > 1$  at low pitch angles, since the inequality  
 268  $K_\mu > \mu$  is satisfied in a sufficiently wide pitch angle range (for all energies for a flat  
 269 packet, for  $W_0 < 2.75$  MeV for a Gaussian packet). Also, because wave amplitude is  
 270 high, the resonant interaction shifts the location of the resonance point: for particles with  
 271 increasing and decreasing pitch angle the resonance point is shifted to the trailing and  
 272 front edge of the packet, respectively. Recall that the sign of pitch angle change depends  
 273 on the initial phase (see Eq.(7)). The value of  $K_\mu$  in (7) thus will also depend on the ini-  
 274 tial phase. As can be seen from Figure 1c, for some pitch angles  $|dK_\mu/d\Theta_{L0}|$  is relatively  
 275 large, so the effects of the nonlinear shift of the resonance point can be significant.

276 With packet propagation away from the equator, the resonance points are shifted  
 277 to higher  $z$ , at the same time they become closer to the trailing edge of the packet. The  
 278 value of  $R$  also changes. For a Gaussian packet, propagation away from the equator shifts  
 279 the location of minimum  $R$  to the lower  $\Theta_L$  and increases its value (for illustration, see  
 280 (Grach & Demekhov, 2018a)). Consecutively,  $R$  decreases for smaller  $\Theta_L$  and increases  
 281 for higher  $\Theta_L$ . For a flat packet, qualitatively the dependence on packet location is the  
 282 same, but quantitatively it is much weaker.

283 Due to a fairly high wave amplitude and the packet being relatively short, the re-  
 284 gion of resonant interaction is determined by the effective packet length. Because of this,  
 285 resonant interaction with packets with different profiles can yield different results even  
 286 when resonance points are located in the middle of the packet (where  $R$  and  $K_\mu$  are the  
 287 same for both packets).

288 Grach and Demekhov (2018a, 2018b) considered a similar wave packet, but with  
 289 a higher electron density  $N_e$ . This leads to a higher refractive index  $n$  which in turn shifts  
 290 the range of resonant electron energies to lower values and noticeably decreases  $R$ . In  
 291 that case, nonlinear regimes  $R \leq 1$  are also possible and effective for a Gaussian wave  
 292 packet.

### 293 *3.1.2 Change in pitch angle in different interaction regimes*

294 The possibility and the comparative influence of various interaction regimes can  
 295 be analyzed based on the phase averaged change of  $\mu = \sin^2 \Theta_L$ . Dependencies  $\langle \Delta\mu \rangle(\Theta_L, W_0)$   
 296 are shown in Figure 2.

297 According to Figure 2, various nonlinear regimes ( $\langle \Delta\mu \rangle \neq 0$ ) are possible in a cho-  
 298 sen range of parameters. Detailed analysis of particle trajectories shows the following.

299 For a Gaussian packet, positive  $\langle \Delta\mu \rangle$  results from combined effect of force bunch-  
 300 ing and nonlinear shift of the resonance point under condition  $dK_\mu/d\Theta_{L0} > 0$ . Force  
 301 bunching dominates for lower pitch angles, when the condition  $K_\mu \geq \mu$  is satisfied for  
 302  $R > 1$ , i.e. quasi-linear estimate (7) formally allows pitch angle decrease to the nega-  
 303 tive values. Under these conditions, force bunching (the second term on the right-hand  
 304 side of (4), which is enhanced when  $p_\perp \rightarrow 0$ ) ensures the physical consistence of the sys-  
 305 tem (2)–(5) solution (the positivity of the first adiabatic invariant) and increases pitch  
 306 angle during resonant interaction. For initial pitch angles near the loss cone, the influ-  
 307 ence of force bunching is so strong, that not only the mean value  $\langle \Delta\mu \rangle > 0$  but also  
 308  $\Delta\mu > 0$  for a single particle with an arbitrary initial phase. For this case, the parti-  
 309 cle trajectories, phase plane and  $\Delta\mu(\Psi_{\text{res}})$  are shown in Figure 3a. Here  $\Psi_{\text{res}}$  is the phase  
 310 at the point of resonance  $\Delta = 0$ , calculated along the real trajectory. Note that the co-  
 311 efficients of the system (2)–(5) depend on time explicitly, i.e., the system is non-autonomous.  
 312 Therefore, the trajectories on the phase plane may intersect (different trajectories reach  
 313 the same point at different times). As one can see, resonance phase can take values from  
 314 a limited range, and doesn't equal the phase at the point  $d\Psi/dt = 0$ .

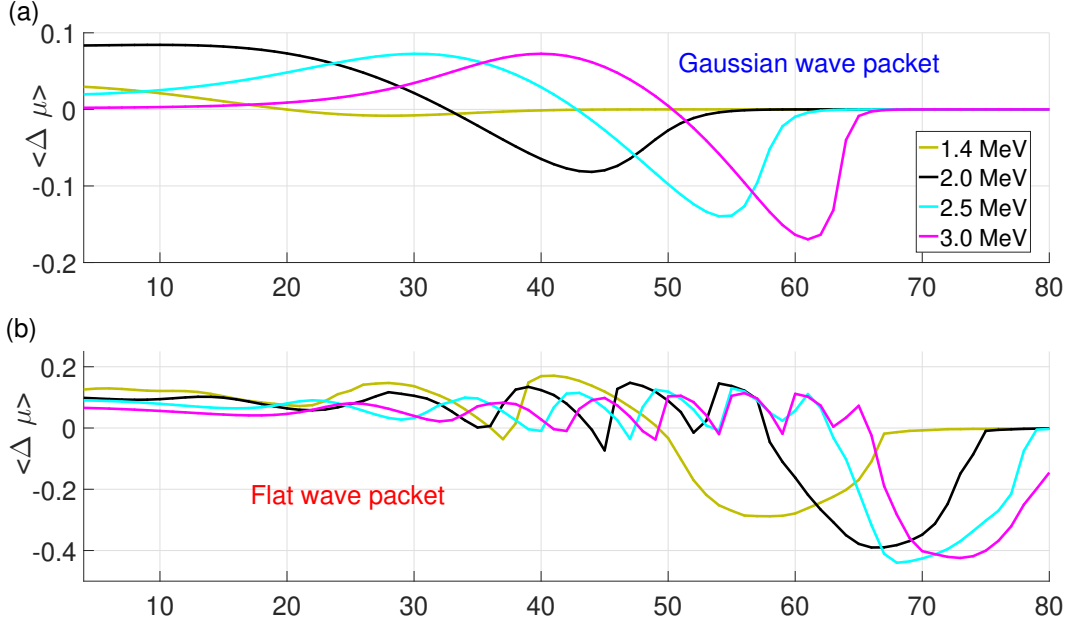


**Figure 2.** Phase averaged change in  $\mu$  for Gaussian (a) and flat (b) wave packets.

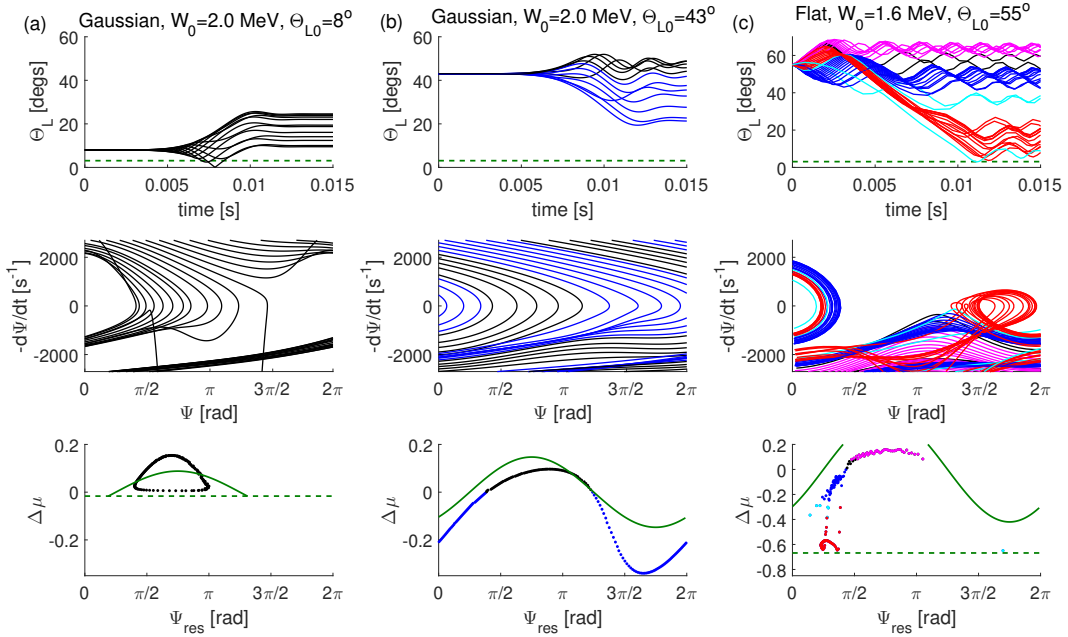


**Figure 3.** Illustration of the possible interaction regimes. Plots in columns a), b), and c) correspond, respectively, to the force bunching, nonlinear shift of the resonance point, and various regimes at  $R < 1$ . Top rows show the oscillograms of  $\Theta_L$ , middle rows show the phase plane, and bottom rows show the  $\Delta\mu$  dependence on the resonance phase. Colors denote types of particle trajectories: black and blue correspond to untrapped particles with  $\Delta\mu > 0$  and  $\Delta\mu < 0$ , respectively, magenta to phase-bunched particles, cyan to directed scattering and red to wave trapping. Green dashed lines in the top and bottom rows indicate loss cone, and green solid lines correspond to quasi-linear estimate (7).

315 In the case when the maximum of  $\langle \Delta\mu \rangle(\Theta_{L0})$  is located at the intermediate pitch  
316 angles ( $W_0 > 2$  MeV), this maximum is caused by the nonlinear shift of the resonance  
317 point under condition  $dK_\mu/d\Theta_{L0} > 0$ . The negative values of  $\langle \Delta\mu \rangle$  are caused by non-  
318 linear shift of the resonance point under condition  $dK_\mu/d\Theta_{L0} < 0$ , i.e. when change  
319 in pitch angle (7) decreases with  $\Theta_{L0}$ . This case is illustrated by Figure 3b. As one can  
320 see, phase portrait of the system is close to the quasi-linear regime, while the dependence  
321  $\Delta\mu(\Psi_{\text{res}})$  differs from estimate (7).

322 Nonlinear regimes corresponding to  $R \leq 1$ , i.e. phase bunching, directed scattering  
323 and particle trapping by the wave field occur for a certain fraction of particles for  
324 energies  $W_0 \geq 2.5$  MeV in the vicinity of the minimum  $\langle \Delta\mu \rangle$  (trapping only takes place  
325 for  $W_0 = 3.0$  MeV).

326 For a flat packet, the region of  $\Theta_{L0} < 30\text{--}35^\circ$  corresponds to the combined effect  
327 of force bunching and nonlinear shift of the resonance point under condition  $dK_\mu/d\Theta_{L0} >$   
328  $0$  (force bunching predominates for lower  $\Theta_{L0}$ ). For the intermediate pitch angles (from  
329  $30\text{--}50^\circ$  for  $W_0 = 1.4$  MeV to  $40\text{--}65^\circ$  for  $W_0 = 3.0$  MeV), the main interaction regimes  
330 are phase bunching (causes local maxima  $\langle \Delta\mu \rangle > 0$ ) and directed scattering (causes  
331 local minima  $\langle \Delta\mu \rangle \approx 0$ ). The smooth global minimum under high  $\Theta_L$  is caused by the  
332 effective wave trapping, though for untrapped particles both phase bunching and directed  
333 scattering can take place. This case is shown in Figure 3c. The global minimum of the  
334 dependence  $\langle \Delta\mu \rangle(\Theta_L)$  for a flat packet corresponds to the unperturbed resonance point  
335 located at the trailing edge of the packet. At higher pitch angles, the unperturbed res-  
336 onance condition is not fulfilled within the packet, but due to nonlinear shift of the res-  
337 onance point, for some particles the resonance condition can be fulfilled; all such par-  
338 ticles are trapped by the wave field. Detailed study of the nonlinear interaction regimes  
339 under  $R < 1$  can be found in (Grach & Demekhov, 2018a, 2018b).

340 With increasing electron energy, the local extrema of  $\langle \Delta\mu \rangle(\Theta_L)$  are shifted to higher  
341  $\Theta_L$ , for both packets. Wave packet propagation away from the equator will shift the lo-  
342 cal extrema of  $\langle \Delta\mu \rangle(\Theta_L)$  to the lower  $\Theta_L$  (same as with  $R(\Theta_L), K_\mu(\Theta_L)$ ).

## 343 **3.2 Precipitation mechanisms and effects of wave packet propagation**

344 Preliminary analysis of particle trajectories shows that precipitation is possible as  
345 a result of either almost quasi-linear interaction, directed scattering or wave trapping.  
346 The range of particle pitch angles for which the precipitation in either regime is possi-  
347 ble is also influenced by force bunching, nonlinear shift of the resonance point and phase  
348 bunching. To study the role of each precipitation mechanism we plot temporal dynam-  
349 ics of ‘scattering’ equatorial pitch angle  $\Theta_{Lsc}$  defined as equatorial pitch angles of pre-  
350 cipitating electrons before the last interaction. Similar analysis was made by Kubota and  
351 Omura (2017), for different wave packet and plasma parameters, but they did not dis-  
352 cuss precipitation for the particles near the loss cone. We also show the distribution of  
353 all precipitating particles over  $\Theta_{Lsc}$ .

### 354 **3.2.1 Gaussian wave packet**

355 The results for a Gaussian wave packet are shown in Figure 4. For the first 3–4 passes  
356 of particles through the wave packet in the resonant direction (which takes about 2 s)  
357 the temporal dynamics is influenced by the initial particle distribution in space. Recall  
358 that at  $t = 0$ , the ensemble of the particles is placed at the trailing edge of the wave  
359 packet. After that, the particles can be considered uniformly distributed between the mir-  
360 ror points. The initial particle location doesn’t influence the distribution of precipitat-  
361 ing particles over the scattering pitch angles.

362 Precipitation is possible only for  $\Theta_{Lsc} \leq 28^\circ$ . For these values, three regimes are  
363 possible: almost quasi-linear regime, force bunching, and nonlinear shift of the resonance

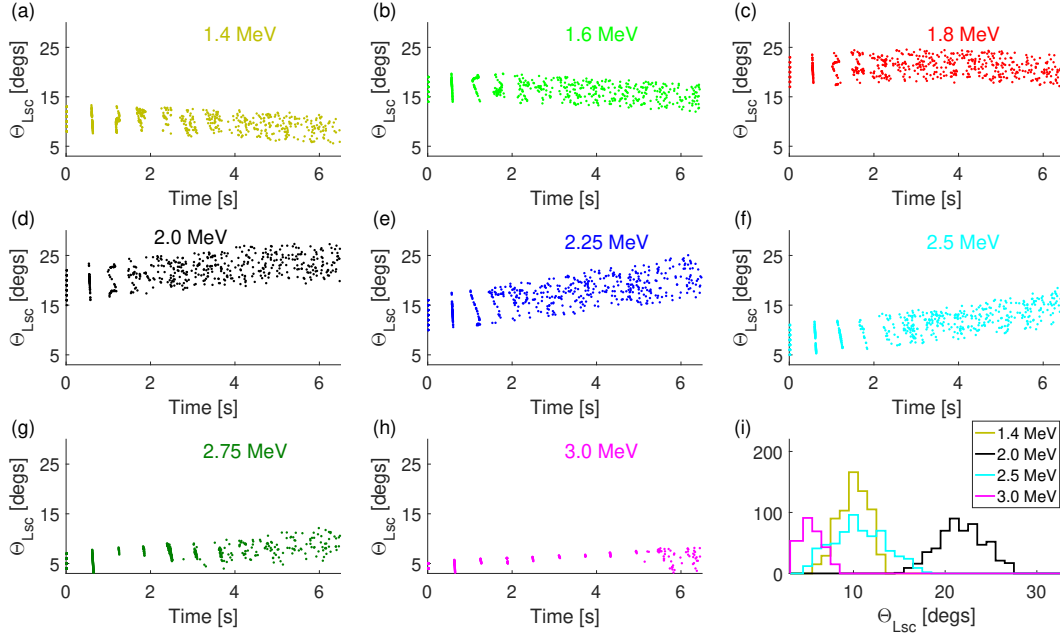


**Figure 4.** Equatorial pitch angles  $\Theta_{Lsc}$  of precipitating electrons before the last interaction with the wave packet as a function of time, for a Gaussian wave packet. Time stamps correspond to particle exiting the wave packet, i.e. approximately a one and a quarter of bounce period  $T_B$  before precipitating. Panel (i) shows the distribution of precipitating particles over  $\Theta_{Lsc}$  during the entire simulation interval.

364 point with  $\langle \Delta\mu \rangle > 0$ . Nonlinear resonance shift with  $\langle \Delta\mu \rangle < 0$  takes place only for  
 365  $\Theta_L \geq 40^\circ$ , which is above  $\Theta_{Lsc}$  range. That means that precipitation in this regime  
 366 is not possible, but particles can be effectively moved to the lower pitch angles (see also  
 367 Figure 3b). As it was mentioned above in Section 3.1.2, the nonlinear regimes under  $R \leq$   
 368 1 take place only for a small fraction of particles and do not have significant effect.

369 For particles with energies 1.6–2.25 MeV, the influence of force bunching is strong  
 370 enough to block precipitation completely for equatorial pitch angles up to  $\Theta_L \approx 15^\circ$ .

371 The range of  $\Theta_{Lsc}$  depends on time for most of the energies. For lower energies,  
 372  $W_0 = 1.4$ – $1.6$  MeV, resonance points for  $\Theta_L < 25^\circ$  at  $t = 0$  are located closer to the  
 373 trailing edge of the packet and for them  $R$  increases and  $K_\mu$  decreases as the packet prop-  
 374 agates (at the time  $t = 0$ , minimum  $R$  is located close to the loss cone). Smaller val-  
 375 ues of  $K_\mu$  correspond to lower initial pitch angles for which estimate (7) gives decreas-  
 376 ing of  $\mu$  below the loss cone value  $\mu_c$  (precipitation in quasi-linear regime) or below zero  
 377 (effective force bunching blocking precipitation). Thus, both maximum and minimum  
 378  $\Theta_{Lsc}$  decrease in this case. For higher energies,  $W_0 = 2.0$ – $3.0$  MeV, the situation is the  
 379 opposite: resonance points for  $\Theta_L < 25^\circ$  at  $t = 0$  are located closer to the front edge  
 380 of the packet, thus  $R$  decreases ( $K_\mu$  increases) as wave packet propagates. Thus, both  
 381 maximum and minimum values of  $\Theta_{Lsc}$  increase.

382 Distributions of precipitated particles over  $\Theta_{Lsc}$  (Figure 4i) have similar profiles  
 383 for all the energies, i.e., they have a smooth maximum in the middle of the  $\Theta_{Lsc}$  range.

### 384 3.2.2 Flat wave packet

385 The temporal dynamics of  $\Theta_{Lsc}$  is shown in Figure 5.

386 For all energies, there is a small number of particles which are scattered into loss  
 387 cone having initial pitch angle that differs from  $\Theta_{Lc}$  by fractions of a degree. The anal-  
 388 ysis of their trajectories shows that these particles precipitate after non-resonant inter-  
 389 action with the wave packet (due to the large amplitude) to conjugated ionosphere. Their  
 390 number is small compared to the total number of precipitating particles, and they do  
 391 not influence any further results.

392 Force bunching blocks precipitation from low pitch angles for all energies, though  
 393 its influence (range of 'blocked' pitch angles) decreases with energy and varies with time.  
 394 Scattering pitch angles  $\Theta_{Lsc} < 45\text{--}50^\circ$  correspond to precipitation after almost quasi-  
 395 linear interaction or directed scattering. High scattering pitch angles correspond to pre-  
 396 cipitation directly caused by wave trapping. For the considered parameters of plasma  
 397 and wave packet, this effect is possible only for energies  $W_0 = 1.4\text{--}1.8$  MeV; with in-  
 398 creasing energy this precipitation starts later in time. It can be explained as follows. For  
 399 higher energies, the region of effective wave trapping is located at higher  $\Theta_L$  (see Fig-  
 400 ure 2b), thus even the same value of  $\langle\Delta\mu\rangle$  is not enough for a particle to precipitate. Wave  
 401 packet propagation shifts the effective wave trapping region to lower pitch angles, which  
 402 makes precipitation possible.

403 Distributions of precipitating particles in pitch angles have different profiles for dif-  
 404 ferent energies. Apart from the very narrow maximum very close to the loss cone, which  
 405 corresponds to the particles precipitated after non-resonant interaction, their structure  
 406 is as follows. For  $W_0 = 1.4\text{--}1.8$  MeV, the distributions have three local maxima: the  
 407 first one (near  $20^\circ$ ) corresponds to quasi-linear regime, and the second (around  $40^\circ$ ) and  
 408 third ( $50\text{--}70^\circ$ ) ones correspond to directed scattering and wave trapping, respectively.  
 409 The 'dip' between the second and the third maxima can also be seen on the temporal  
 410 dynamics panels. It corresponds to the region where phase bunching prevails (recall that  
 411 phase bunching results in a pitch-angle increase). For energies  $W_0 = 2.0\text{--}3.0$  MeV, pre-  
 412 cipitation is mostly caused by quasi-linear regime, though precipitation by directed scat-  
 413 tering is also possible for a number of particles.

414 The smooth variations of scattering pitch angle range (for quasi-linear regime) are  
 415 connected with fluctuations in  $\langle\Delta\mu\rangle(\Theta_L)$ ; wave packet propagation will shift the local  
 416 extrema of  $\langle\Delta\mu\rangle(\Theta_L)$ .

#### 417 **4 Pitch Angle Distribution and Precipitating Fluxes**

418 In the further analysis of the simulation results, the total simulation time 6.5 s is  
 419 divided into 11 intervals  $\{\Delta t_i\} = t_{i+1} - t_i$ ,  $i = 0, 1, \dots, 11$ ,  $t_0 = 0$ , where  $\Delta t_0 = 0.2$  s  
 420 and the subsequent intervals  $\Delta t_{0 < i < 11} = 0.6$  s. The latter value corresponds to the bounce  
 421 period of particles close to the loss cone:  $T_B(\Theta_L = \Theta_{Lc}) \approx 0.62\text{--}0.64$  s. Since at the  
 422 initial time  $t = 0$  all electrons are located at the trailing edge of the wave packet, the  
 423 first time interval  $\Delta t_0 = 0.2$  s was chosen slightly longer than the time  $T_B(\Theta_L = \Theta_{Lc})/4 \approx$   
 424  $0.15$  s after which a particle near the loss cone reaches the ionosphere. Since  $\Delta t_0 < T_B(\Theta_L =$   
 425  $80^\circ) \approx 0.33$  s we can say that during  $\Delta t_0$  all particles passed the wave packet in res-  
 426 onant direction only once. We average the particle distribution function and the precip-  
 427 itating flux over the intervals  $\Delta t_i$  and attribute the obtained result to the time  $T_i = (t_{i+1} +$   
 428  $t_i)/2$  (the middle of the interval  $\Delta t_i$ ).

429 To analyze the simulation results in terms of particle distribution function and to  
 430 compare obtained precipitating fluxes with quasi-linear estimates, we have to establish  
 431 the connection between the distribution function  $\Phi_{\Theta_L}(\Theta_L)$  (or  $\Phi_\mu(\mu)$ ) and the distribu-  
 432 tion of the test particles in the phase space. This procedure is described in detail in the  
 433 Appendix.

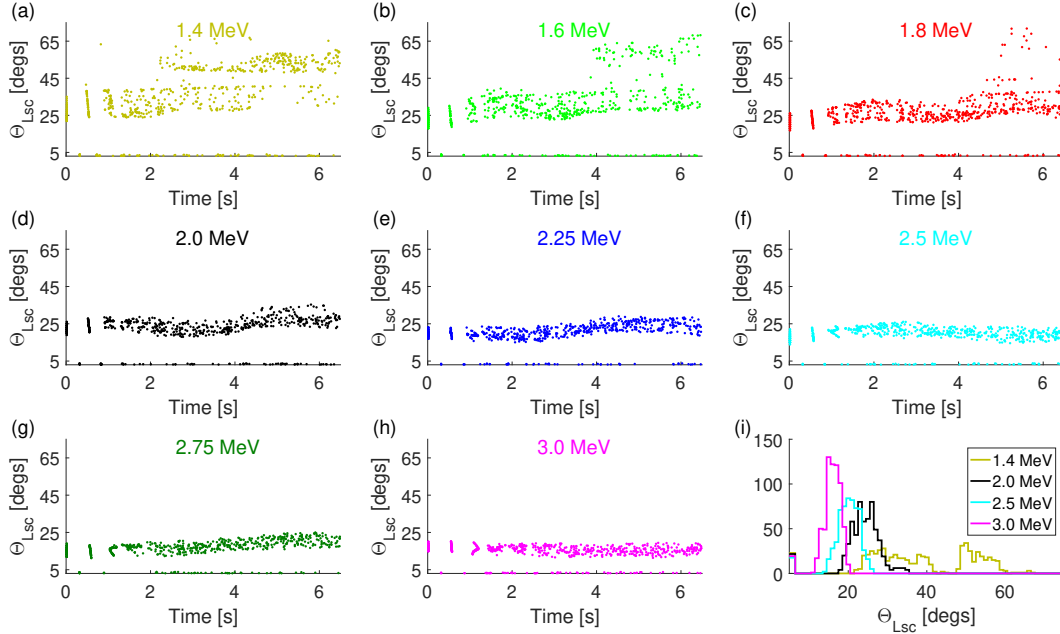


**Figure 5.** Same as in Figure 4, but for a flat packet.

434

#### 4.1 Evolution of pitch angle distribution

435

436

The particles distribution function  $\Phi_{\Theta_L}(\Theta_L)$  for both wave packets for several energy values at several times  $T_i$  is shown in Figure 6.

437

438

439

440

441

442

443

For a flat packet, the distribution function dynamics is qualitatively similar for all the energies considered. For the low equatorial pitch angles near the loss cone, the distribution function is either close to isotropic (with a value slightly lower than the initial value  $\Phi_{\Theta_L}^0$ ; this value decreases slightly with increasing energy), or it has a local maximum in the loss cone. In most cases, the global maximum of the distribution function is located at the pitch angles  $60\text{--}70^\circ$  and is equal to the initial value  $\Phi_{\Theta_L}(\Theta_L)$  or slightly exceeds it.

444

445

446

447

448

449

450

451

452

For a Gaussian packet, for intermediate energies  $W_0 = 1.8\text{--}2.25$  MeV and not high pitch angles  $\Theta_L \leq 60^\circ$  the distribution function almost coincides with the distribution function for a flat packet. The similar behavior of distribution functions for both packets corresponds to the resonance points for particles with intermediate pitch angles located in the middle of the wave packet. For higher energies  $2.75\text{--}3.0$  MeV, the distribution function increases from small value  $\Phi_{\Theta_L}^c$  to the initial value  $\Phi_{\Theta_L}^0$  at pitch angles  $\Theta_L \approx 15\text{--}20^\circ$ . For higher pitch angles,  $\Phi_{\Theta_L}$  fluctuates. For energies  $1.4$  and  $2.5$  MeV, at different time moments the distribution function can have a local maximum in the loss cone, be close to isotropic or gradually increase from  $\Phi_{\Theta_L}^c$  to the initial value  $\Phi_{\Theta_L}^0$ .

453

454

455

456

457

458

459

460

461

The main difference between flat and Gaussian wave packets is observed for high pitch angles  $\Theta_L > 60^\circ$ , because for this range the resonance points are located near the trailing edge of the packet. For a Gaussian packet, due to very small values of wave amplitude at these points there is no resonant interaction for these pitch angles, and the distribution function remains constant. For a flat packet, firstly, small fluctuations of  $\Theta_L$  are possible even when the exact resonance condition is not fulfilled within the packet, and secondly, due to nonlinear shift of the resonance point, a fraction of particles may be trapped by the wave field, which results in large pitch angle decrease and leads to the appearance of 'dips' in the distribution function in the corresponding region.

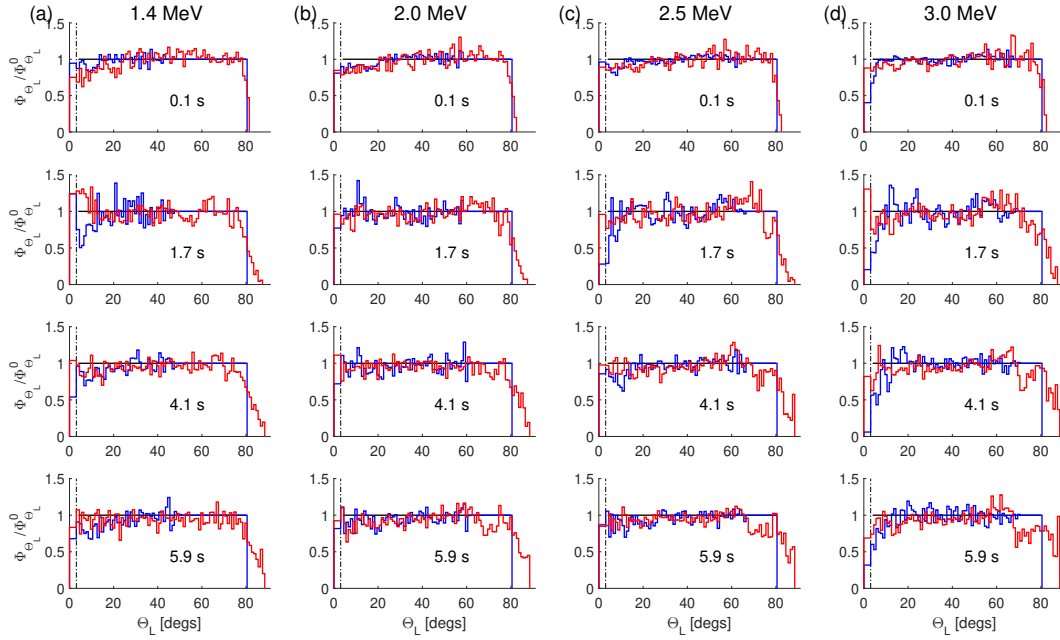


**Figure 6.** The evolution of pitch angle distribution for a Gaussian packet (blue lines) and a flat packet (red lines). Solid black line shows the initial distribution  $\Phi_{\Theta_L}|_{t=0} = \text{const} = \Phi_{\Theta_L}^0$ , dash-dotted black line indicates  $\Theta_{Lc}$ .

462

## 4.2 Precipitating fluxes

463

464

465

466

467

To analyze the precipitating fluxes  $S_{\text{pr}}^{\text{num}}$ , directly corresponding to the numerical simulation results, we normalize them to the flux  $S_{\text{pr}}^{\text{SD}}$  in the limiting case of strong diffusion. In this case the loss cone is filled continuously and distribution function is isotropic; the precipitating flux takes the limiting value equal to the trapped flux (Kennel & Petschek, 1966; Bespalov & Trakhtengerts, 1986; Trakhtengerts & Rycroft, 2008):

$$S_{\text{pr}}^{\text{SD}} = \frac{N\mu_c}{\bar{T}_B}. \quad (11)$$

468

469

Here  $N$  is the total number of particles in geomagnetic field tube with unit cross section at the ionosphere,  $\bar{T}_B = \int T_B(\mu)d\mu$ ,  $\mu_c$  corresponds to the loss cone.

470

471

472

473

474

475

476

In the case when distribution function  $\Phi_\mu(\mu)$  is not isotropic and doesn't have maximum in the loss cone (i.e., has a finite positive derivative  $\partial\Phi_\mu/\partial\mu$ ), it is possible to obtain quasi-linear estimates of precipitating fluxes  $S_{\text{pr}}^{\text{lin}}$ . For this, we use the smooth approximation  $\Phi_\mu^{\text{sm}}(\mu)$  of numerically obtained distribution function. The root mean square deviation of  $\mu$  that determines the diffusion coefficient is calculated using both the analytical estimate (10) and numerical results (A15). Calculation algorithms for both  $S_{\text{pr}}^{\text{num}}$  and  $S_{\text{pr}}^{\text{lin}}$  can be found in the Appendix.

477

478

479

480

Since for a flat packet the distribution function is either close to isotropic or has a local maximum in the loss cone, quasi-linear estimates of precipitating flux  $S_{\text{pr}}^{\text{lin}}$  were calculated only for a Gaussian packet and only for those times when the derivative of the distribution function in the vicinity of loss cone was not close to zero.

481

482

483

484

The normalized precipitating fluxes  $\tilde{S}$  are shown in the Figures 7 and 8 for Gaussian and flat packet, respectively. To avoid the influence of the initial spatial bunching of the particles, we exclude the first time interval  $\Delta t_0 = 0-0.2$  s and average over several sequent time intervals, when this influence is significant (see Figures 4 and 5).

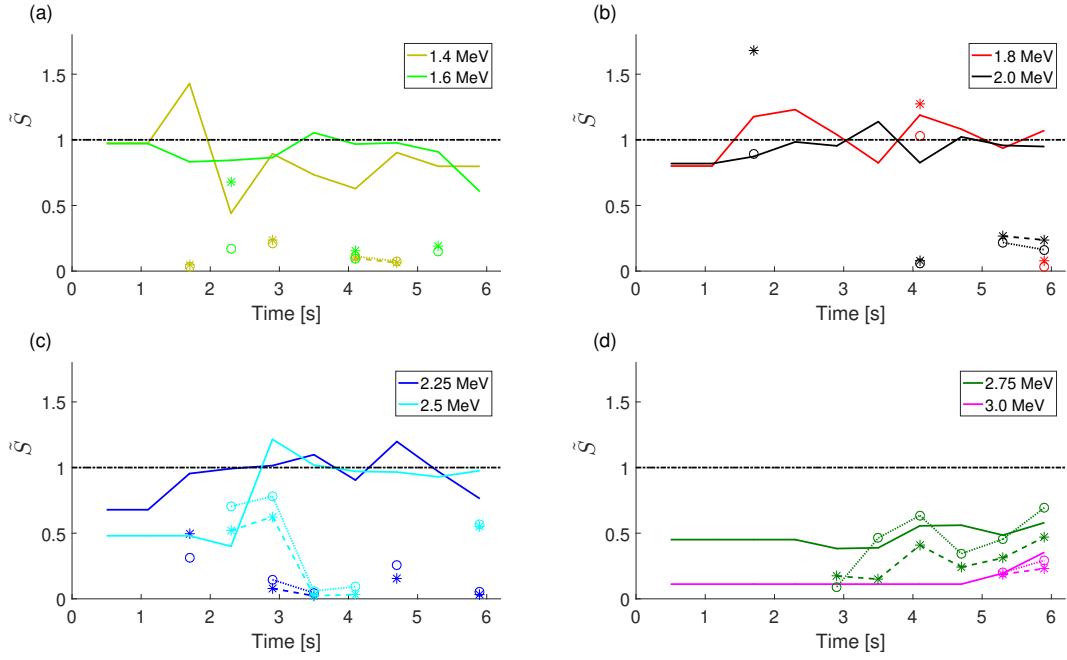


**Figure 7.** Precipitating fluxes for a Gaussian packet: normalized precipitating flux  $S_{\text{pr}}^{\text{num}}/S_{\text{pr}}^{\text{SD}}$  (solid lines) and quasi-linear flux  $S_{\text{pr}}^{\text{lin}}/S_{\text{pr}}^{\text{SD}}$ , calculated using diffusion coefficient based on theoretical estimate (10) (dashed lines and star markers) and simulation results (A15) (dotted lines and circle markers).

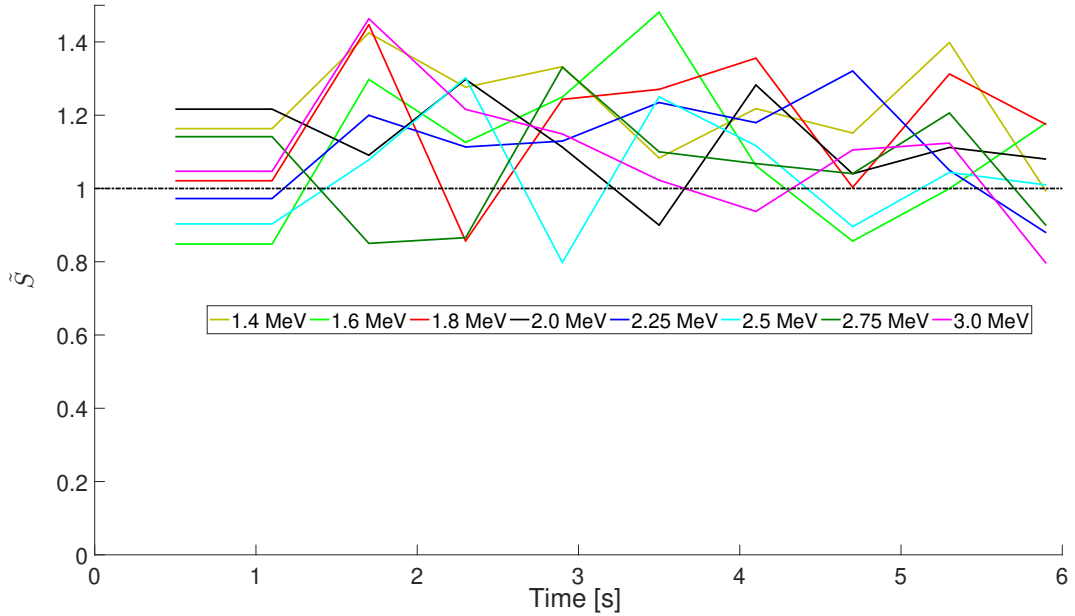


**Figure 8.** Normalized precipitating fluxes  $S_{\text{pr}}^{\text{num}}/S_{\text{pr}}^{\text{SD}}$  for a flat packet.

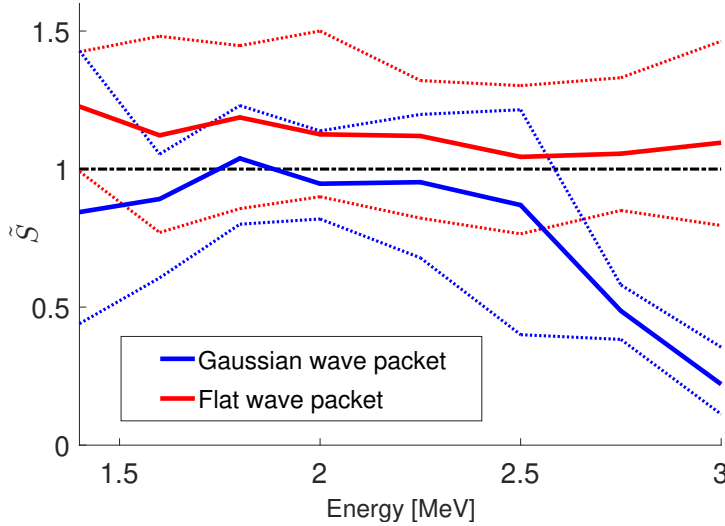


**Figure 9.** Normalized precipitating fluxes, averaged (solid lines), maximized (dotted lines) and minimized (dotted lines) over the simulation time. Red color corresponds to a flat wave packet, blue color corresponds to a Gaussian wave packet.

485 The dynamics of precipitating fluxes corresponds to the dynamics of the distribu-  
 486 tion function. For a flat packet, the flux  $S_{\text{pr}}^{\text{num}}$  fluctuates near the limiting flux  $S_{\text{pr}}^{\text{SD}}$ :  $S_{\text{pr}}^{\text{num}} =$   
 487  $(0.8\text{--}1.5)S_{\text{pr}}^{\text{SD}}$ . The fluxes exceeding the limiting value correspond to nonmonotonic dis-  
 488 tribution function having a local maximum in the loss cone.

489 Precipitating fluxes, averaged over simulation time, as well as maximum and mini-  
 490 mum values, are shown in Figure 9. The largest values of  $S_{\text{pr}}^{\text{num}}/S_{\text{pr}}^{\text{SD}}$  correspond to the  
 491 energy 1.4 MeV, the smallest ones correspond to 2.5–3.0 MeV. In general, the depen-  
 492 dence of maximum/minimum and average fluxes on the energy is weak and nonmono-  
 493 tonic (see Figure 9). Such a dependence clearly indicates the competition between two  
 494 nonlinear regimes, which have opposite effects on pitch angle dynamics, but the same  
 495 energy dependence. Recall that force bunching blocks precipitation from low pitch an-  
 496 gles, while wave trapping can directly cause precipitation from high pitch angles; the in-  
 497 fluence of both regimes decreases with increasing energy.

498 For a Gaussian packet, dependence of normalized flux  $S_{\text{pr}}^{\text{num}}/S_{\text{pr}}^{\text{SD}}$  on energy and  
 499 time is much stronger. The maximum values of  $S_{\text{pr}}^{\text{num}}/S_{\text{pr}}^{\text{SD}}$  correspond to intermediate  
 500 energies  $W_0 = 1.6\text{--}2.0$  MeV. In this case, like in the case of a flat packet,  $S_{\text{pr}}^{\text{num}}$  fluctu-  
 501 ates near  $S_{\text{pr}}^{\text{SD}}$ , though its maximum values are smaller:  $S_{\text{pr}}^{\text{num}} = (0.8\text{--}1.2)S_{\text{pr}}^{\text{SD}}$ . For  
 502 lower energy  $W_0 = 1.4$  MeV normalized precipitating flux has a maximum over time;  
 503 for higher energies  $W_0 = 2.25\text{--}3.0$  MeV precipitating flux decreases with energy and  
 504 increases with time (for  $W_0 = 2.25\text{--}2.5$  MeV, it quickly increases to  $S_{\text{pr}}^{\text{num}}/S_{\text{pr}}^{\text{SD}} \approx 1$ ).  
 505 This temporal dynamics and dependence on energy follows the dynamics of resonant in-  
 506 teraction effectiveness (the value of  $R$ ) at low (‘scattering’ range) pitch angles.

507 In most cases, analytical and numerical values of the root mean square change in  
 508  $\mu$  ((10) and (A15), respectively) are close to each other (see Figure A2). That means that  
 509 theoretical estimate (10) can be valid even in the case of strong nonlinear effects and  $\langle \Delta\mu \rangle \neq$   
 510 0. Correspondingly, quasi-linear estimates of the precipitating flux obtained by using ei-  
 511 ther (10) or (A15) give similar results. In contrast to this fact, the fluxes  $S_{\text{pr}}^{\text{lin}}$  are close  
 512 to the simulated flux  $S_{\text{pr}}^{\text{num}}$  only for energies  $W_0 = 2.75\text{--}3.0$  MeV and at some moments  
 513 for  $W_0 = 2.5; 2.0; 1.8$  MeV. Note that the moments with  $S_{\text{pr}}^{\text{lin}} > S_{\text{pr}}^{\text{SD}}$  (Figure 7b,  $W_0 =$   
 514 2.0 and 1.8 MeV) correspond to overestimated analytical diffusion (10) in the case of strong

515 force bunching (see Figure A2b). In all other cases,  $S_{\text{pr}}^{\text{lin}} \ll S_{\text{pr}}^{\text{num}}$ . The low values of quasi-  
 516 linear estimates are caused by the following. The smoothed distribution function, which  
 517 is used for calculating the quasi-linear precipitating flux (see Appendix, Figure A1), in  
 518 these cases is virtually isotropic, while the original distribution function, obtained in the  
 519 simulation, has a local maximum in the loss cone, which can't be described by the dif-  
 520 fusion equation.

521 It's interesting to note that for energies  $W_0 \leq 2.5$  MeV even in the cases when  
 522  $\Phi_\mu$  increases monotonically from the loss cone, quasi-linear estimates can be also much  
 523 smaller than the fluxes obtained directly from the simulation results. Most likely, it is  
 524 explained by the following factors. Quasi-linear estimates for the precipitating flux are  
 525 obtained by the averaging over bounce oscillations; this approach can be used when change  
 526 in  $\mu$  during one bounce period (as a result of one resonant interaction) is relatively small.  
 527 With considered parameters of plasma and wave packets, for energies  $W_0 < 2.75$  MeV  
 528 and low pitch angles (scattering pitch angles range)  $\Delta\mu \sim \mu$  and overall number of bounce  
 529 oscillations is not large. In this case, averaging over bounce oscillations can lead to in-  
 530 correct results.

## 531 5 Discussion and Conclusions

532 The precipitating fluxes are formed as a result of several interaction regimes with  
 533 opposite effects. The influence of each regime depends on wave packet characteristics and  
 534 electron energy.

535 Under considered parameters of plasma and wave packets, particle trapping by the  
 536 wave field is not very effective, but the role of nonlinear regimes with inhomogeneity pa-  
 537 rameter  $R \geq 1$  is significant.

538 The effect of force bunching (the Lorentz force term in Eq. (4) for the particle phase)  
 539 on the resonant interaction is rarely discussed in analytical studies. Lundin and Shkliar  
 540 (1977) analyzed motion of resonance electrons with low transverse velocities in the field  
 541 of a whistler mode parallel propagating wave. They showed that when wave amplitude  
 542 is high enough, force bunching leads to systematic increase in electron pitch angle. Our  
 543 simulation shows similar results for electrons interacting with EMIC waves: force bunch-  
 544 ing leads to pitch angle increase for particles with very low pitch angles near the loss cone.  
 545 In most part of the considered energy range ( $W_0 = 1.6$ – $2.25$  MeV for a Gaussian wave  
 546 packet and  $W_0 < 3$  MeV for the flat wave packet) force bunching blocks the precipi-  
 547 tation completely from a noticeable range of equatorial pitch angles (up to  $15^\circ$  and  $25^\circ$   
 548 for the Gaussian and flat wave packets, respectively). The significance of the force bunch-  
 549 ing influence is connected with a relatively low electron plasma density; the latter results  
 550 in low refractive index, which in turn leads to large change in equatorial pitch angle when  
 551  $R > 1$  and trapping by the wave field is not possible. Under different plasma conditions,  
 552 as reported by Kubota and Omura (2017), force bunching can lead to strong equatorial  
 553 pitch angle decrease for particles released from the wave trapping.

554 Shift of the resonance point is another nonlinear effect which is important under  
 555 considered conditions when  $R > 1$ . For low equatorial pitch angles  $\Theta_L \leq 30$ – $40^\circ$ , non-  
 556 linear shift of the resonance point leads to an average increase of the pitch angle. For  
 557 higher pitch angles, this effect takes place only for a Gaussian wave packet and has the  
 558 opposite sign, i.e. pitch angle decreases. This decrease does not directly cause precipi-  
 559 tation, but particles can be moved to the pitch angles where almost quasi-linear diffu-  
 560 sion takes place and precipitation occurs.

561 Three nonlinear regimes are possible for inhomogeneity parameter  $R < 1$ : phase  
 562 bunching (pitch angle increase for a large number of untrapped particles), directed scat-  
 563 tering (strong pitch angle decrease for a small number of untrapped particles) and par-  
 564 ticle trapping by the wave field (also leads to pitch angle decrease in our case). For a Gaus-

565 sian wave packet and considered parameters, these regimes are possible only for higher  
 566 energies 2.75–3.0 MeV and in a narrow range of pitch angles, so they do not play a sig-  
 567 nificant role. For a flat wave packet, precipitation as a result of directed scattering and  
 568 wave trapping is possible for  $W_0 = 1.4$ – $1.8$  MeV. For higher energies, directed scatter-  
 569 ing and wave trapping move particles to the pitch angle range of quasi-linear scattering.  
 570 Phase bunching blocks precipitation from intermediate equatorial pitch angles and moves  
 571 particles into the region of effective wave trapping.

572 It is important to note that, even when the nonlinear precipitation is most effec-  
 573 tive (flat packet,  $W_0 = 1.4$  MeV, see Figure 5), the number of 'nonlinearly' precipitated  
 574 particles doesn't exceed the number of the particles precipitated in almost quasi-linear  
 575 regime. The situation will be different for a plasma with higher cold electron density (Kubota  
 576 & Omura, 2017; Grach & Demekhov, 2018a, 2018b), when the inhomogeneity param-  
 577 eter takes smaller values, and directed scattering and wave trapping are more effective.  
 578 In that case, nonlinear precipitation will be possible for a Gaussian wave packet (Grach  
 579 & Demekhov, 2018a, 2018b), and precipitating fluxes will be formed mostly by combined  
 580 effect of wave trapping and directed scattering (Kubota & Omura, 2017).

581 To analyze the precipitating fluxes, we have normalized the precipitating fluxes to  
 582 the flux value in the case of strong diffusion, which corresponds to continuous filling of  
 583 the loss cone, i.e. isotropic distribution function in the vicinity of the loss cone. Max-  
 584 imum normalized fluxes (in the entire energy range for a flat packet, and  $W_0 = 1.8$ –  
 585  $2.25$  MeV for a Gaussian packet) are close in value and fluctuate near strong diffusion  
 586 flux. In these cases, distribution function in the vicinity of the loss cone is close to isotropic;  
 587 there are also moments in which distribution function has a maximum in the loss cone.

588 For a flat packet, the normalized flux averaged over the simulation time almost doesn't  
 589 depend on energy. This results from the competition of nonlinear regimes with mutu-  
 590 ally opposite effects (force bunching and wave trapping) whose strength decreases with  
 591 energy.

592 For a Gaussian packet, the time-averaged normalized flux has a maximum over en-  
 593 ergy. The stronger dependence on particle energy for a Gaussian packet is caused by the  
 594 different amplitude values at different resonance points. Maximum normalized fluxes are  
 595 reached for  $W_0 = 1.8$ – $2.25$  MeV; in this case, the resonance points for particles with  
 596 'scattering' pitch angles are located near the middle of the packet. For lower energies ( $W_0 =$   
 597  $1.4$ – $1.6$  MeV) the resonance points for 'scattering' particles are located near the trail-  
 598 ing edge of the packet. In this case, the normalized fluxes increase with energy. For higher  
 599 energies 2.5–3.0 MeV (the resonance points for 'scattering' particles are located near the  
 600 front edge of the packet) the normalized fluxes increase with time and decrease with en-  
 601 ergy. The temporal dynamics and energy dependence of the precipitating fluxes and 'scat-  
 602 tering' pitch angles range for lower and higher energy follows the dynamics of inhom-  
 603 ogeneity parameter  $R$  at low ('scattering' range) pitch angles.

604 The results show that dynamics of nonlinear regimes and their role in the forma-  
 605 tion of precipitating flux can strongly depend on the amplitude profile of the wave packet.  
 606 Any difference from the constant amplitude (flat packet) will result in stronger depen-  
 607 dence of the precipitating flux on particle energy within the resonant range.

608 We have compared the precipitating fluxes, obtained in the simulation, with the-  
 609 oretical quasi-linear estimates. For the parameters where quasi-linear equations for the  
 610 distribution function are applicable, the simulated fluxes are close to theoretical estimates.  
 611 This is true for higher energies ( $W_0 = 2.75$ – $3.0$  MeV) for a Gaussian packet. In other  
 612 cases, including the ones where precipitating fluxes are formed under  $R \geq 1$ , i.e., when  
 613 no trapping is possible, simulated precipitating fluxes exceed theoretical estimates by a  
 614 factor from 2 to more than 10.

We obtained that pitch angle distribution function is isotropic in the wide range of parameters. This is consistent with observations by low Earth orbit satellites, in which precipitating and trapped fluxes of relativistic electrons are often close or equal to each other (Yahnin et al., 2016, 2017). However, the detailed comparison with the observational data requires a separate study; in particular, the wave packet fine structure has to be taken into account, similar to the approach used by Tao et al. (2012, 2013) for chorus emissions. That study is planned for the future work.

In conclusion, we briefly summarize the main results of this study.

1. The force bunching can completely block the precipitation from low equatorial pitch angles.
2. For the major part of the considered parameter domain, the pitch angle distribution is close to isotropic in the vicinity of the loss cone.
3. The precipitating fluxes are formed as a result of several interaction regimes with opposite effects. For higher energies (2.75–3.0 MeV in the considered case), theoretical quasi-linear estimates are applicable, and the simulated fluxes are close to them. For lower energies, simulated precipitating fluxes exceed theoretical estimates by a factor from 2 to more than 10. This result is important for using quasi-linear diffusion fluxes in numerical modelling of radiation belts.

## Appendix A Calculation of the Pitch Angle Distribution Function and Precipitating Fluxes

Most of the expressions below follow Besselov and Trakhtengerts (1986); Trakhtengerts and Rycroft (2008) and are given here for the reader's benefit.

Let  $f$  be the particle distribution function averaged over gyrophases. If the pitch angle and energy change during one bounce oscillation is not very large, then the distribution function  $F$  averaged over bounce oscillation period  $T_B$  is close to the local distribution function  $f$ :

$$F = \frac{1}{T_B} \int f dt \approx \frac{1}{T_B} \int f \frac{dz}{v_{||}} \approx f. \quad (\text{A1})$$

Total number of particles in a geomagnetic flux tube with unit cross section at the ionosphere can be calculated as

$$N = \int n(z) \frac{B_{0m}}{B_0(z)} dz. \quad (\text{A2})$$

Here  $n(z) = \int f d^3\mathbf{p} = \int f \sin \Theta d\Theta p^2 dp d\Psi$  is the local number density,  $\Theta$  is the local pitch angle, and  $B_{0m}$  is the maximum field for the given geomagnetic field line.

From expressions (A1) and (A2) we can obtain:

$$N = \frac{1}{2\mu_c} \int 2T_B F_{\Theta_L}(\Theta_L) \cos \Theta_L \sin \Theta_L d\Theta_L p^2 dp d\Psi = \frac{1}{2\mu_c} \int T_B F_\mu(\mu) d\mu p^2 dp d\Psi. \quad (\text{A3})$$

Here  $F_{\Theta_L}$  is the distribution function  $F$  written as a function of  $\Theta_L$  and  $F_\mu$  is the distribution function  $F$  written as a function of  $\mu$ :  $F_{\Theta_L}(\Theta_L) = F_\mu(\mu = \sin^2 \Theta_L)$ . The value  $\mu_c = \sin^2 \Theta_{Lc} = B_{0L}/B_{0m}$  corresponds to the loss cone.

The particle energy change during the resonant interaction with EMIC waves is insignificant, so we can consider particles with  $W_0 = \text{const}$ . Then we can use for every energy:

$$F = \frac{\delta(p - p_0)}{p_0^2} \tilde{F}_{\Theta_L}(\Theta_L, \Psi) = \frac{\delta(p - p_0)}{p_0^2} \tilde{F}_\mu(\mu, \Psi), \quad (\text{A4})$$

652 where  $p_0$  is the particle momentum. Integrating (A3) over  $\Psi$  and  $p$  with account of (A4),  
 653 we obtain

$$N = \frac{v_0}{2\mu_c} \int \tilde{\Phi}_{\Theta_L} T_B 2 \cos \Theta_L \sin \Theta_L d\Theta_L = \frac{v_0}{2\mu_c} \int \tilde{\Phi}_\mu T_B d\mu. \quad (\text{A5})$$

654 Here  $v_0 = p_0/(m\gamma)$ ,

$$\tilde{\Phi}_{\Theta_L} = \int \tilde{F}_{\Theta_L}(\Theta_L, \Psi) d\Psi; \quad \tilde{\Phi}_\mu = \int \tilde{F}_\mu(\mu, \Psi) d\Psi. \quad (\text{A6})$$

655 In order to connect the number  $N_p$  of particles in the simulation with  $N$ , we use  
 656 the following normalization:

$$N = \frac{v_0 \bar{T}_B}{2\mu_c} \beta_V N_p, \quad (\text{A7})$$

657 where  $\bar{T}_B = \int T_B(\mu) d\mu$ ,  $\beta_V$  is the normalization constant, and  $N_p$  is the number of par-  
 658 ticles in the simulation.

659 Using (A7), we can write the connection between distribution functions  $\tilde{\Phi}_\mu$  and  $\tilde{\Phi}_{\Theta_L}$   
 660 and distribution of the test particles in the phase space as follows:

$$\tilde{\Phi}_{\Theta_L} = \frac{\Delta N_p \bar{T}_B}{\Delta \Theta_L T_B} \frac{\beta_V}{\sin(2\Theta_L)}; \quad (\text{A8})$$

661

$$\tilde{\Phi}_\mu = \frac{\Delta N_p \bar{T}_B}{\Delta \mu T_B} \beta_V. \quad (\text{A9})$$

662 Here  $\Delta N_p$  is the number of particles having the pitch angle  $\Theta_L$  within the range  $\Delta \Theta_L$   
 663 (in (A8)) and  $\mu$  in the range of  $\Delta \mu$  (in (A9)).

664 If the initial distribution of test particles in  $\Theta_L$  is uniform and equal weight is as-  
 665 signed to each particle, then initial distribution function  $\tilde{\Phi}_{\Theta_L}|_{t=0}$  is not constant. At the  
 666 same time, each particle corresponds to the phase space element  $\Delta \Gamma = \sin(2\Theta_L) \Delta \Theta_L \Delta \Psi =$   
 667  $\Delta \mu \Delta \Psi$ , which does not change during the distribution function evolution. For a more  
 668 correct analysis of simulation results, instead of the initial function  $\tilde{\Phi}_{\Theta_L}|_{t=0}$  we use the  
 669 'weighted' distribution function  $\Phi_{\Theta_L}|_{t=0} = \alpha_w(\Theta_{L0}) \tilde{\Phi}_{\Theta_L}|_{t=0} = \text{const}$ , where  $\alpha_w(\Theta_{L0})$   
 670 are the weights assigned to each particle with initial equatorial pitch angle  $\Theta_{L0}$ . The weights  
 671 are calculated from the condition that the functions  $\Phi_{\Theta_L}|_{t=0}$  and  $\tilde{\Phi}_{\Theta_L}|_{t=0}$  have the same  
 672 normalization.

673 To analyze the simulation results we divide the pitch angle values, corresponding  
 674 to the moments  $t_{i+1} < t \leq t_i$ ,  $0 \leq i \leq 11$  into the intervals  $\Delta \Theta_{Lk}$  ( $\Delta \Theta_{L1} = \Theta_{Lc}$ ,  $\Delta \Theta_{L1,2,\dots} =$   
 675  $1^\circ$ ). Every particle is counted with the weight  $\alpha_w(\Theta_{L0})$ , corresponding to its initial equa-  
 676 torial pitch angle  $\Theta_{L0}$ . To obtain the value of the distribution function in the loss cone,  
 677 we count the particles which were scattered in the loss cone during the current time in-  
 678 terval  $\Delta t_i$ . The obtained distribution function is attributed to the time  $T_i = (t_{i+1} +$   
 679  $t_i)/2$ .

680 The effect of quasi-linear pitch angle diffusion on the averaged distribution func-  
 681 tion is described by the following equation (Bespalov & Trakhtengerts, 1986; Trakhtengerts  
 682 & Rycroft, 2008):

$$\frac{\partial F_\mu}{\partial t} = \frac{1}{T_B} \frac{\partial}{\partial \mu} \left[ \mu \bar{D} \frac{\partial F_\mu}{\partial \mu} \right]. \quad (\text{A10})$$

683 Here  $\bar{D} = \int D dt = \int D ds/v_{||}$ ,  $D$  is the diffusion coefficient, and the integral is taken  
 684 over the interval of bounce averaging. The diffusion coefficient is calculated as

$$D = \frac{(\langle \Delta \Theta_L \rangle_{\text{rms}})^2}{\Delta t}. \quad (\text{A11})$$

685 Here  $\langle \Delta \Theta_L \rangle_{\text{rms}} = \sqrt{\langle (\Delta \Theta_L - \langle \Delta \Theta_L \rangle)^2 \rangle}$  is the root mean square deviation of  $\Theta_L$  dur-  
 686 ing the time interval  $\Delta t$ . Hence,  $\bar{D} = (\langle \Delta \Theta_L \rangle_{\text{rms}})^2$ . We consider one wave packet along

687 the field line, so during a bounce period the particle's pitch angle changes only once, as  
 688 it passes through the wave packet parallel to the wave.

689 The simulated precipitating flux is evaluated as:

$$S_{\text{pr}}^{\text{num}} = \frac{N\delta N_{\text{p}}}{\Delta t}. \quad (\text{A12})$$

690 Here  $\delta N_{\text{p}} = N_{\text{p,lost}}/N_{\text{p}}$  is the relative number of particles, precipitated during time in-  
 691 terval  $\Delta t$ .

692 The particle flux through the loss cone boundary caused by the quasi-linear dif-  
 693 fusion can be estimated by integrating (A10) and taking into account the absence of par-  
 694 ticle sources and sinks at  $\mu = 0$  and  $\mu = 1$ :

$$S_{\text{pr}}^{\text{lin}} = \frac{v_0 \overline{D}}{2} \frac{\partial \Phi}{\partial \mu} \Big|_{\mu=\mu_c} = \frac{v_0}{2} \frac{(\langle \Delta \mu \rangle_{\text{rms}})^2}{4\mu_c} \frac{\partial \Phi_{\mu}}{\partial \mu} \Big|_{\mu=\mu_c}. \quad (\text{A13})$$

695 Here  $\langle \Delta \mu \rangle_{\text{rms}} \approx \sqrt{4\mu(1-\mu)} \langle \Delta \Theta_L \rangle_{\text{rms}}$  is root mean square deviation of  $\mu$  after one res-  
 696 onant interaction in the vicinity of the loss cone  $\mu = \mu_c$ ,  $\sqrt{1-\mu_c} \approx 1$ . The derivative  
 697  $\partial \Phi_{\mu}/\partial \mu|_{\mu=\mu_c}$  can be estimated using distribution function  $\Phi_{\mu}$ , obtained in the simula-  
 698 tion. Analyzing the simulation results, particles with all phase values are summed up,  
 699 which corresponds to phase averaging.

700 To obtain distribution function derivative  $\partial \Phi_{\mu}/\partial \mu$ , which can be used in (A13),  
 701 we use a smooth approximation of the numerical distribution function. For a Gaussian  
 702 wave packet, we choose the following approximation

$$\Phi_{\mu}^{\text{sm}} = \Phi_1 + \Phi_2 \tanh[\Phi_3(\mu - \mu^{\text{sm}})]. \quad (\text{A14})$$

703 Coefficients  $\Phi_1$ ,  $\Phi_2$ ,  $\Phi_3$  and  $\mu^{\text{sm}}$  are found by nonlinear least squares method under the  
 704 conditions  $\Phi_2 > 0$  and  $\Phi_3 > 0$ . To eliminate the influence of the initial spatial distri-  
 705 bution of the particles, we average distribution functions  $\Phi_{\mu}$  over several first time in-  
 706 tervals, when such influence is significant (see Figures 4 and 5). Approximation (A14)  
 707 is shown in Figure A1.

708 Root mean square deviation  $\langle \Delta \mu \rangle_{\text{rms}}$  can be calculated in two ways. One approach  
 709 corresponds to analytical estimate by the stationary phase method  $\langle \Delta \mu \rangle_{\text{rms}}^{\text{lin}}$  (10), and  
 710 the other approach is based on using the numerical results:

$$\langle \Delta \mu \rangle_{\text{rms}}^{\text{num}} = \sqrt{\langle (\Delta \mu^{\text{num}} - \langle \Delta \mu \rangle_{\text{rms}}^{\text{num}})^2 \rangle}. \quad (\text{A15})$$

711 Root mean square deviations, calculated as a function of  $\mu$ , are shown in Figure A2. For  
 712 calculating  $\langle \Delta \mu \rangle_{\text{rms}}^{\text{num}}$  (A15),  $\mu$  is divided in intervals equivalent to step  $1^\circ$  in  $\Theta_L$ . For ev-  
 713 ery energy  $W_0$  and time moment  $T_i$  we find the point  $\mu^*$ , for which  $\langle \Delta \mu \rangle_{\text{rms}}(\mu^*) \approx 2(\mu^* -$   
 714  $\mu_c)$  (in Figure A1, these points are shown by vertical lines). To calculate the quasi-linear  
 715 precipitating flux (A13), we use the diffusion coefficient corresponding to  $\langle \Delta \mu \rangle_{\text{rms}}(\mu^*)$   
 716 and evaluate  $\partial \Phi_{\mu}/\partial \mu$  at  $\mu^*$  by using (A14).

717 By analyzing the results for different subsets of particles we found that a numer-  
 718 ical uncertainty of our calculations is about 10 %.

## 719 Acknowledgments

720 The study conducted in this paper is theoretical and no data was used. This work was  
 721 supported by the Russian Science Foundation, grant 15-12-20005.

## 722 References

723 Albert, J. M. (1993). Cyclotron resonance in an inhomogeneous magnetic field.  
 724 *Physics of Fluids B*, 5(8), 2744–2750. doi: 10.1063/1.860715

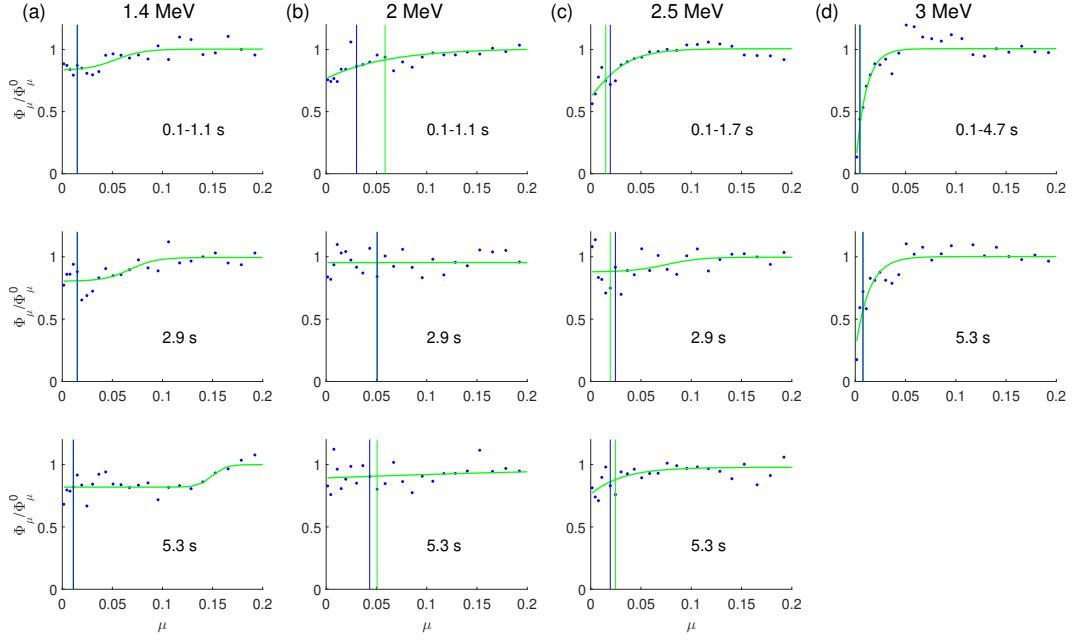


**Figure A1.** Distribution function, obtained in simulation (blue dots), and approximation (A14) (green lines). Vertical lines correspond to the points  $\mu_*$ , calculated for  $\langle \Delta \mu \rangle_{\text{rms}}^{\text{lin}}$  (green) and  $\langle \Delta \mu \rangle_{\text{rms}}^{\text{num}}$  (blue). The top panels correspond to distribution function, averaged over several first time intervals.

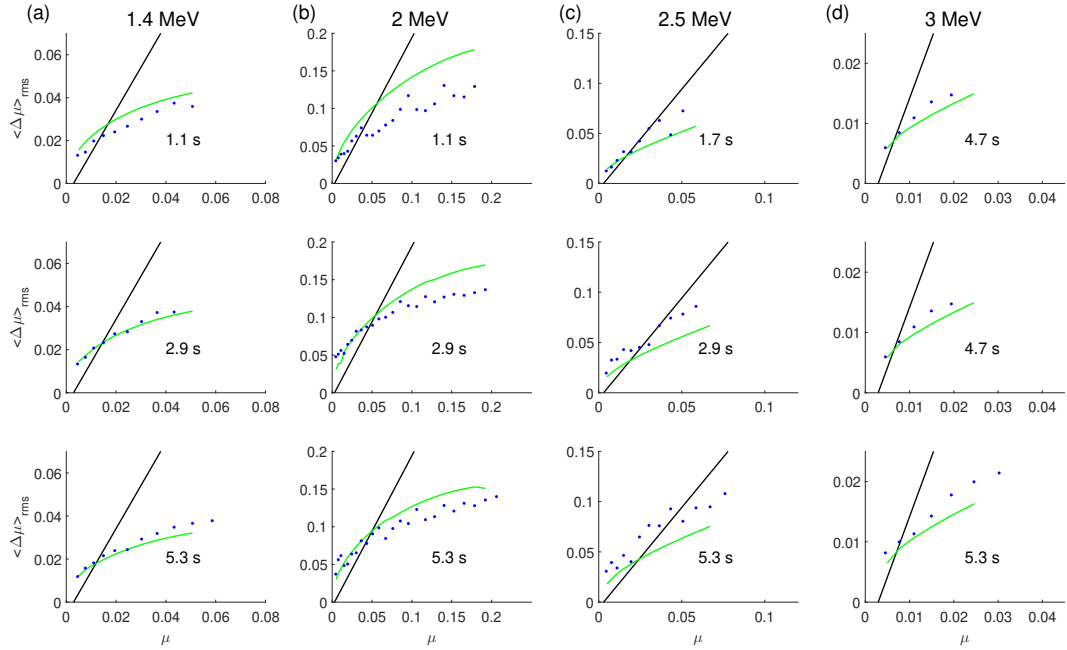


**Figure A2.** Root mean square deviations  $\langle \Delta \mu \rangle_{\text{rms}}^{\text{lin}}$  (green lines) and  $\langle \Delta \mu \rangle_{\text{rms}}^{\text{num}}$  (blue dots). Black lines correspond to  $2(\mu - \mu_c)$ .

- 725 Albert, J. M. (2000). Gyroresonant interactions of radiation belt particles with  
 726 a monochromatic electromagnetic wave. *J. Geophys. Res. Space Physics*,  
 727 *105*(A9), 21191–21209. doi: 10.1029/2000JA000008
- 728 Albert, J. M., & Bortnik, J. (2009). Nonlinear interaction of radiation belt electrons  
 729 with electromagnetic ion cyclotron waves. *Geophys. Res. Lett.*, *36*(12), L12110.  
 730 doi: 10.1029/2009GL038904
- 731 Anderson, B. J., & Hamilton, D. C. (1993). Electromagnetic ion cyclotron waves  
 732 stimulated by modest magnetospheric compressions. *J. Geophys. Res. Space*  
 733 *Physics*, *98*(A7), 11369–11382. doi: 10.1029/93JA00605
- 734 Artemyev, A., Neishtadt, A. I., Vainchtein, D., Vasiliev, A. A., Vasko, I., & Ze-  
 735 lenyi, L. (2018). Trapping (capture) into resonance and scattering on  
 736 resonance: Summary of results for space plasma systems. *Communica-*  
 737 *tions in Nonlinear Science and Numerical Simulation*, *65*, 111–160. doi:  
 738 10.1016/j.cnsns.2018.05.004
- 739 Artemyev, A. V., Mourenas, D., Agapitov, O. V., Vainchtein, D. L., Mozer, F. S., &  
 740 Krasnoselskikh, V. (2015). Stability of relativistic electron trapping by strong  
 741 whistler or electromagnetic ion cyclotron waves. *Physics of Plasmas*, *22*(8),  
 742 082901. doi: 10.1063/1.4927774
- 743 Artemyev, A. V., Neishtadt, A. I., Vasiliev, A. A., & Mourenas, D. (2017). Probabilistic  
 744 approach to nonlinear wave-particle resonant interaction. *Phys. Rev. E*,  
 745 *95*(2), 023204. doi: 10.1103/PhysRevE.95.023204
- 746 Belyaev, P. P., Kotik, D. S., Mityakov, S. N., Polyakov, S. V., Rapoport, V. O., &  
 747 Trakhtengerts, V. Y. (1987). Generation of electromagnetic signals at combi-  
 748 nation frequencies in the ionosphere. *Radiophysics and Quantum Electronics*,  
 749 *30*(2), 189–206. doi: 10.1007/BF01034491
- 750 Belyayev, P. P., Polyakov, S. V., Rapoport, V. O., & Trakhtengerts, V. Y. (1984).  
 751 Fine structure of Alfvén maser radiation. *USSR Report Earth Sciences JPRS*  
 752 *UES*, *24*(2), 138.
- 753 Bespalov, P. A., & Trakhtengerts, V. Y. (1986). The cyclotron instability in the  
 754 Earth radiation belts. In M. A. Leontovich (Ed.), *Reviews of plasma physics*  
 755 (Vol. 10, pp. 155–293). Plenum Publ., N.Y.
- 756 Demekhov, A. G. (2007). Recent progress in understanding Pc1 pearl formation. *J.*  
 757 *Atmos. Sol. Terr. Phys.*, *69*(14), 1609–1622. doi: 10.1016/j.jastp.2007.01.014
- 758 Demekhov, A. G., Trakhtengerts, V. Y., Rycroft, M. J., & Nunn, D. (2006).  
 759 Electron acceleration in the magnetosphere by whistler-mode waves of  
 760 varying frequency. *Geomagnetism and Aeronomy*, *46*(6), 711–716. doi:  
 761 10.1134/S0016793206060053
- 762 Engebretson, M. J., Keiling, A., Fornacon, K.-H., Cattell, C. A., Johnson, J. R.,  
 763 Posch, J. L., ... Rème, H. (2007). Cluster observations of Pc 1.2 waves  
 764 and associated ion distributions during the October and November 2003  
 765 magnetic storms. *Planetary and Space Science*, *55*(6), 829–848. doi:  
 766 10.1016/j.pss.2006.03.015
- 767 Engebretson, M. J., Posch, J. L., Westerman, A. M., Otto, N. J., Slavin, J. A., Le,  
 768 G., ... Lessard, M. R. (2008). Temporal and spatial characteristics of pc1  
 769 waves observed by st5. *J. Geophys. Res. Space Physics*, *113*(A7), A07206. doi:  
 770 10.1029/2008JA013145
- 771 Engebretson, M. J., Posch, J. L., Wygant, J. R., Kletzing, C. A., Lessard, M. R.,  
 772 Huang, C.-L., ... Shiokawa, K. (2015). Van Allen probes, NOAA, GOES,  
 773 and ground observations of an intense EMIC wave event extending over 12 h in  
 774 magnetic local time. *J. Geophys. Res. Space Physics*, *120*(7), 5465–5488. doi:  
 775 10.1002/2015JA021227
- 776 Fraser, B. J., & Nguyen, T. S. (2001). Is the plasmopause a preferred source region  
 777 of electromagnetic ion cyclotron waves in the magnetosphere? *J. Atmos. Sol.*  
 778 *Terr. Phys.*, *63*(11), 1225–1247. doi: 10.1016/S1364-6826(00)00225-X
- 779 Grach, V. S., & Demekhov, A. G. (2018a). Resonance interaction of relativistic

- 780 electrons with ion-cyclotron waves. i. specific features of the nonlinear interac-  
 781 tion regimes. *Radiophysics and Quantum Electronics*, 60(12), 942–959. doi:  
 782 10.1007/s11141-018-9860-0
- 783 Grach, V. S., & Demekhov, A. G. (2018b). Resonant interaction of relativistic  
 784 electrons with electromagnetic ion–cyclotron waves. ii. integral parameters of  
 785 interaction regimes. *Radiophysics and Quantum Electronics*, 61(6), 389–401.  
 786 doi: 10.1007/s11141-018-9900-9
- 787 Jordanova, V. K., Albert, J., & Miyoshi, Y. (2008). Relativistic electron precipi-  
 788 tation by emic waves from self-consistent global simulations. *J. Geophys. Res.*  
 789 *Space Physics*, 113(A3), A00A10. doi: 10.1029/2008JA013239
- 790 Kangas, J., Guglielmi, A., & Pokhotelov, O. (1998). Morphology and physics of  
 791 short-period magnetic pulsations. *Space Science Reviews*, 83, 435–512.
- 792 Karpman, V. I., Istomin, Y. N., & Shklyar, D. R. (1974). Nonlinear theory  
 793 of a quasimonochromatic whistler mode packet in inhomogeneous plasma.  
 794 *Plasma Phys.*, 16(8), 685–703.
- 795 Keika, K., Takahashi, K., Ukhorskiy, A. Y., & Miyoshi, Y. (2013). Global char-  
 796 acteristics of electromagnetic ion cyclotron waves: Occurrence rate and its  
 797 storm dependence. *J. Geophys. Res. Space Physics*, 118(7), 4135–4150. doi:  
 798 10.1002/jgra.50385
- 799 Kennel, C. F., & Petschek, H. E. (1966). Limit on Stably Trapped Particle Fluxes.  
 800 *J. Geophys. Res.*, 71(1), 1–28. doi: 10.1029/JZ071i001p00001
- 801 Kubota, Y., & Omura, Y. (2017). Rapid precipitation of radiation belt electrons  
 802 induced by emic rising tone emissions localized in longitude inside and out-  
 803 side the plasmopause. *J. Geophys. Res. Space Physics*, 122(1), 293–309. doi:  
 804 10.1002/2016JA023267
- 805 Loto’Aniu, T. M., Fraser, B. J., & Waters, C. L. (2005). Propagation of electromag-  
 806 netic ion cyclotron wave energy in the magnetosphere. *J. Geophys. Res. Space*  
 807 *Physics*, 110(A7), A07214. doi: 10.1029/2004JA010816
- 808 Lundin, B. V., & Shklyar, D. R. (1977). Interaction of electrons with low trans-  
 809 verse velocities with VLF waves in an inhomogeneous plasma. *Geomagnetism*  
 810 *and Aeronomy*, 17(2), 246–251.
- 811 Millan, R. M., & Thorne, R. (2007). Review of radiation belt relativistic electron  
 812 losses. *J. Atmos. Sol. Terr. Phys.*, 69(3), 362–377. doi: 10.1016/j.jastp.2006.06  
 813 .019
- 814 Morley, S. K., Friedel, R. H. W., Cayton, T. E., & Noveroske, E. (2010). A rapid,  
 815 global and prolonged electron radiation belt dropout observed with the global  
 816 positioning system constellation. *Geophys. Res. Lett.*, 37(6), L06102. doi:  
 817 10.1029/2010GL042772
- 818 Mursula, K. (2007). Satellite observations of Pc 1 pearl waves: The chang-  
 819 ing paradigm. *J. Atmos. Sol. Terr. Phys.*, 69(14), 1623–1634. doi:  
 820 10.1016/j.jastp.2007.02.013
- 821 Omura, Y., Pickett, J., Grison, B., Santolik, O., Dandouras, I., Engebretson, M., . . .  
 822 Masson, A. (2010). Theory and observation of electromagnetic ion cyclotron  
 823 triggered emissions in the magnetosphere. *J. Geophys. Res. Space Physics*,  
 824 115(A7), A07234. doi: 10.1029/2010JA015300
- 825 Omura, Y., & Zhao, Q. (2012). Nonlinear pitch angle scattering of relativistic  
 826 electrons by emic waves in the inner magnetosphere. *J. Geophys. Res. Space*  
 827 *Physics*, 117(A8), A08227. doi: 10.1029/2012JA017943
- 828 Omura, Y., & Zhao, Q. (2013). Relativistic electron microbursts due to nonlin-  
 829 ear pitch angle scattering by emic triggered emissions. *J. Geophys. Res. Space*  
 830 *Physics*, 118(8), 5008–5020. doi: 10.1002/jgra.50477
- 831 Pickett, J. S., Grison, B., Omura, Y., Engebretson, M. J., Dandouras, I., Masson,  
 832 A., . . . Constantinescu, D. (2010). Cluster observations of EMIC triggered  
 833 emissions in association with Pc1 waves near Earth’s plasmopause. *Geophys.*  
 834 *Res. Lett.*, 37(9), L09104. doi: 10.1029/2010GL042648

- 835 Santolik, O., Gurnett, D., Pickett, J., Parrot, M., & Cornilleau-Wehrlin, N. (2003).  
 836 Spatio-temporal structure of storm-time chorus. *J. Geophys. Res. Space*  
 837 *Physics*, *108*(A7), 1278. doi: 10.1029/2002JA009791
- 838 Shoji, M., Omura, Y., Grison, B., Pickett, J., Dandouras, I., & Engebretson, M.  
 839 (2011). Electromagnetic ion cyclotron waves in the helium branch induced  
 840 by multiple electromagnetic ion cyclotron triggered emissions. *Geophys. Res.*  
 841 *Lett.*, *38*(17), L17102. doi: 10.1029/2011GL048427
- 842 Shprits, Y. Y., Chen, L., & Thorne, R. M. (2009). Simulations of pitch angle scatter-  
 843 ing of relativistic electrons with ml<sub>t</sub>-dependent diffusion coefficients. *J. Geo-*  
 844 *phys. Res. Space Physics*, *114*(A3), A03219. doi: 10.1029/2008JA013695
- 845 Summers, D., & Thorne, R. M. (2003). Relativistic electron pitch-angle scatter-  
 846 ing by electromagnetic ion cyclotron waves during geomagnetic storms. *J. Geo-*  
 847 *phys. Res. Space Physics*, *108*(A4), 1143. doi: 10.1029/2002JA009489
- 848 Tao, X., Bortnik, J., Albert, J. M., Thorne, R. M., & Li, W. (2013). The importance  
 849 of amplitude modulation in nonlinear interactions between electrons and large  
 850 amplitude whistler waves. *J. Atmos. Sol. Terr. Phys.*, *99*, 67–72. (Dynamics of  
 851 the Complex Geospace System) doi: 10.1016/j.jastp.2012.05.012
- 852 Tao, X., Bortnik, J., Thorne, R. M., Albert, J. M., & Li, W. (2012). Effects of  
 853 amplitude modulation on nonlinear interactions between electrons and chorus  
 854 waves. *Geophys. Res. Lett.*, *39*(6), L06102. doi: 10.1029/2012GL051202
- 855 Thorne, R. M., & Kennel, C. F. (1971). Relativistic electron precipitation during  
 856 magnetic storm main phase. *J. Geophys. Res.*, *76*(19), 4446–4453. doi: 10  
 857 .1029/JA076i019p04446
- 858 Trakhtengerts, V., & Demekhov, A. (2007). Generation of Pc 1 pulsations in the  
 859 regime of backward wave oscillator. *J. Atmos. Sol. Terr. Phys.*, *69*(14), 1651–  
 860 1656. doi: 10.1016/j.jastp.2007.02.009
- 861 Trakhtengerts, V. Y. (1995). Magnetosphere cyclotron maser: Backward wave os-  
 862 cillator generation regime. *J. Geophys. Res.*, *100*(A9), 17205–17210. doi: 10  
 863 .1029/95JA00843
- 864 Trakhtengerts, V. Y., & Rycroft, M. J. (2008). *Whistler and Alfvén mode cyclotron*  
 865 *masers in space*. New York: Cambridge University Press.
- 866 Usanova, M. E., Mann, I. R., Bortnik, J., Shao, L., & Angelopoulos, V. (2012).  
 867 Themis observations of electromagnetic ion cyclotron wave occurrence: Depen-  
 868 dence on ae, symh, and solar wind dynamic pressure. *J. Geophys. Res. Space*  
 869 *Physics*, *117*(A10), A10218. doi: 10.1029/2012JA018049
- 870 Yahnin, A. G., Titova, E. E., Demekhov, A. G., Yahnina, T. A., Popova, T. A.,  
 871 Lyubchich, A. A., . . . Raita, T. (2019). Simultaneous observations of elf/vlf  
 872 and emic waves and energetic particle precipitation during multiple magneto-  
 873 spheric compressions. *Geomagnetism and Aeronomy*, *59*(6), 668–680.
- 874 Yahnin, A. G., Yahnina, T. A., Raita, T., & Manninen, J. (2017). Ground pul-  
 875 sation magnetometer observations conjugated with relativistic electron  
 876 precipitation. *J. Geophys. Res. Space Physics*, *122*(9), 9169–9182. doi:  
 877 10.1002/2017JA024249
- 878 Yahnin, A. G., Yahnina, T. A., Semenova, N. V., Gvozdevsky, B. B., & Pashin,  
 879 A. B. (2016). Relativistic electron precipitation as seen by noaa poes. *J.*  
 880 *Geophys. Res. Space Physics*, *121*(9), 8286–8299. doi: 10.1002/2016JA022765